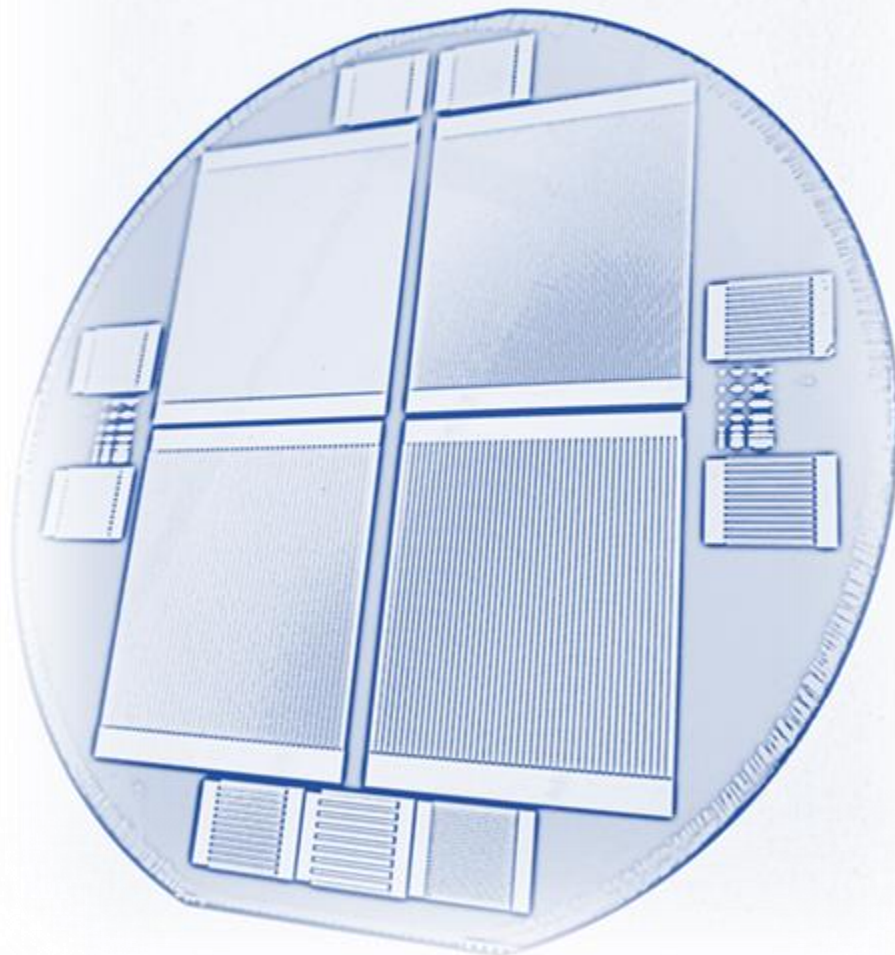


High efficiency IBC c-Si solar cells with poly-Si passivating contacts

Yue Zhang

Delft University of Technology



Acknowledgement

First of all, I would like to thank my supervisor Dr. Olindo Isabella for giving me chance to do my master thesis project in PVMD group. I thank you for pushing me forward and teaching me what an eligible researcher should be.

I would like to convey my gratitude to and my daily supervisor Dr. Guangtao Yang. I thank you for giving me so much help during my thesis project. I appreciate your wisdom and calmness, you can always give a brief and profound answer to my question, I learnt so much both for basic physics knowledge and for experimental skills. You inspire me on both my work and my further life.

My thanks and appreciation also to Gianluca Limodio for your advice and the help you gave me in the lab. You shared me your research experience and you are such an interesting person that bring happy to our life.

I would like to thank Dr. Paul Procel for your support and discussion, and teaching me lots of knowledge.

Hao Ge and Jiali Zhou, you are my best friends from the beginning I came to the Netherlands. I am so lucky to meet and work with you guys. I appreciate the life we went through during this two years and the discussion we had about the study and life, which will be my precious memory.

I enjoy working with my fellow students: Camilla Massacesi and Yvar de Groot for the discussion and the funny time we had. Furthermore, I would like to thank the whole PVMD group and people in EKL for the help I received. And I would also like to thank the presence of all my thesis committee members.

Last but not the least, I would like to express my greatest gratitude to my parents and all my friends. Thank you for supporting me and giving me a colorful life.

Yue Zhang
Delft, June 2017

List of Publications

Journal article

Guangtao Yang, Yue Zhang, Paul Procel, Arthur Weeber, Olindo Isabella, Miro Zeman, Poly-Si(O)_x passivating contacts for high-efficiency c-Si IBC Solar cell, Energy Procedia, accepted for publication.

Abstract

Crystalline silicon (c-Si) solar cells based on the polycrystalline silicon (poly-Si) passivating contact is becoming one of the most promising solar cell structures that enable high efficiency due to the minimization of metal contact recombination. The interdigitated back contact (IBC) crystalline silicon (c-Si) solar cells based on poly-Si passivating contacts is investigated in this thesis. The optimization of IBC solar cells with poly-Si passivating contacts, in this work, is focused on two aspects: (1) the enhanced passivation of poly-Si passivating contacts, and (2) the optimized front surface passivation. The optimization of poly-Si passivating contacts is investigated from the following three aspects: (1) the implantation dose of poly-Si as back surface field (BSF) and emitter, (2) the annealing condition to the ion-implanted poly-Si, and (3) the formation of tunnel oxide. Experimental results, obtained with symmetrical test structures, show that the J_0 for n-type poly-Si samples achieved 4.5 fA/cm^2 with implied V_{oc} higher than 730 mV. For p-type poly-Si samples, J_0 is 12.9 fA/cm^2 and implied V_{oc} is 714 mV. The optimization of front surface is achieved by optimizing the front surface field (FSF) ion-implantation dose and the passivation layers with double-sided textured n-type float zone wafers with symmetrical structure. The optimized J_0 for the FSF, implanted with the dose of $1 \times 10^{14} / \text{cm}^2$, is as low as 6.5 fA/cm^2 which is covered by a-Si:H/SiN_x stack. The deposition conditions for a-Si:H and SiN_x are 22nm at 250 °C and 75 nm at 400 °C, respectively. After the application of above mentioned improvements, the efficiency of our IBC poly-Si passivating contacts solar cells has reached 21.9% for 9 cm² cell and 22.5% for 0.72 cm² cell. Meanwhile, the highest FF of 83.2% achieved with 0.72 cm² cell shows the high efficiency potential of our solar cells.

Key words: IBC crystalline silicon solar cell, poly-crystalline silicon passivating contact, tunneling oxide, ion-implantation.

CONTENTS

ACKNOWLEDGEMENT	I
LIST OF PUBLICATIONS	III
ABSTRACT	V
NOMENCLATURE	IX
LIST OF FIGURES	XIII
LIST OF TABLES.....	XV
1 INTRODUCTION	1
1.1 BACKGROUND	1
1.2 THE BASIC WORKING PRINCIPLE OF A SOLAR CELL AND CHARACTERIZATION.....	2
1.2.1 Basic working principle of a solar cell	2
1.2.2 External Solar cell parameters and external quantum efficiency	3
1.3 RECOMBINATION MECHANISM & PASSIVATION	5
1.3.1 Recombination mechanisms	5
1.3.2 Passivation mechanisms.....	6
1.4 CONCEPTS OF HIGH-EFFICIENCY C-Si SINGLE JUNCTION SOLAR CELL.....	7
1.4.1 Homo-junction solar cells	7
1.4.2 Solar cells with carrier selective passivating contacts	8
1.4.3 The interdigitated back contact solar cell	10
1.5 OBJECTIVE AND THESIS OUTLINE	11
2 EXPERIMENT.....	13
2.1 INTRODUCTION.....	13
2.2 POLY-Si PASSIVATING CONTACTS.....	14
2.3 FRONT SURFACE PASSIVATION	14
2.4 SOLAR CELL FABRICATION.....	15
2.5 MEASUREMENT EQUIPMENT.....	16
2.5.1 Dark I-V measurement	16
2.5.2 Photo-conductance lifetime measurement	17
2.5.3 External quantum efficiency measurement.....	18
2.5.4 Current density-voltage measurement	19
3 OPTIMIZATION OF POLY-Si PASSIVATING CONTACTS	21

3.1	OPTIMIZATION OF IMPLANTATION DOSE	21
3.2	EFFECT OF ANNEALING ON POLY-SI PASSIVATION.....	24
3.3	OPTIMIZATION OF TUNNEL SiO ₂	27
3.4	SOLAR CELLS.....	30
4	OPTIMIZATION OF FRONT SURFACE PASSIVATION	33
4.1	OPTIMIZATION OF FSF PASSIVATION	33
4.2	SOLAR CELLS.....	35
4.3	SOLVING THE SHUNT IN SOLAR CELL	36
4.4	REDUCE THE A-SI:H PARASITIC ABSORPTION	38
4.5	THE INFLUENCE OF POST ANNEALING ON CELL PERFORMANCE.....	39
5	CONCLUSIONS AND RECOMMENDATIONS.....	43
5.1	CONCLUSION	43
5.2	RECOMMENDATIONS	44
	BIBLIOGRAPHY	49

Nomenclature

α	absorption coefficient
Δn	Excess carrier density
η	Efficiency
λ	Wavelength
Φ_{ph}	Photon flux density
τ_{Auger}	Auger lifetime
τ_{Bulk}	Bulk lifetime
τ_{eff}	Effective minority carrier lifetime
$\tau_{radiative}$	Radiative lifetime
τ_{SRH}	Shockley-Read-Hall lifetime
$\tau_{Surface}$	Surface lifetime
ν	Frequency of the light
c	Light speed, $2.998 \times 10^8 \text{ m/s}$
e	Electron
E	Energy
E_C	The lowest energy of conduction band
E_G	Bandgap energy
E_V	The highest energy of valence band
FF	Fill factor
G	Generation rate
h	Plank constant, $6.625 \times 10^{-34} \text{ J} \cdot \text{s}$
$i-V_{oc}$	Implied open-circuit voltage
I	Current
I_{ph}	Photo-generated current
I_{sc}	Short-circuit current
J_0	Dark saturation current density under thermal equilibrium
J_0^{BSF}	Dark saturation current density at back surface field
J_0^{Bulk}	Dark saturation current density in bulk
$J_0^{emitter}$	Dark saturation current density at emitter
J_0^{FSF}	Dark saturation current density at front surface field
J_{MPP}	Current density at maximum power point
J_{ph}	Photo-generated current density
J_{sc}	Short-circuit current density

k	Boltzmann constant, $1.38 \times 10^{-23} \text{ J/K}$
L_N	Minority carrier diffusion length for electrons in p-type region
L_P	Minority carrier diffusion length for holes in n-type region
n	Ideality factor
n_i	Intrinsic carrier density
N_D	Dopant density
P_{in}	Incident power
P_{MPP}	Maximum power point
q	Elementary charge, $1.602 \times 10^{-19} \text{ C}$
R_S	Series resistance
R_{sh}	Shunt resistance
T	Temperature in Kelvin
V_{OC}	Open-circuit voltage
V_{MPP}	Voltage at maximum power point
W	Depletion region width
Al	Aluminum
ALD	Atomic layer deposition
Al_2O_3	Aluminum oxide
AM	Air mass
ARC	Anti-reflection coating
a-Si	Amorphous silicon
a-Si:H	Hydrogenated amorphous silicon
a-SiN _x :H	Hydrogenated amorphous silicon nitride
B	Boron
BHF	Buffered hydrofluoric acid
BJBC	Back junction back contact
BSF	Back surface field
c-Si	Crystalline silicon
DI	Deionized
e-h	electron-hole pair
EQE	External quantum efficiency
FSF	Front surface field
FZ	Float zone
GaAs	Gallium Arsenide

HJT	Heterojunction
HNO ₃	Nitric acid
IBC	Interdigitated back contact
IEA	International energy agency
J-V	Current-density Voltage
LID	Light induced degradation
LPCVD	Low pressure chemical vapor deposition
NAOS	Nitric acid oxidation of silicon
NH ₃	Ammonia
O ₂	Oxygen
P	Phosphorous
PECVD	Plasma enhanced chemical vapor deposition
PERC	Passivated emitter rear cell
PERL	Passivated emitter rear local diffused
POLO	Polycrystalline on oxide
Poly-Si	Polycrystalline silicon
PV	Photovoltaic
QSSPC	Quasi-steady state photo-conductance
R	Reflectance
SiH ₄	Silane
SiN _x	Silicon nitride
SiO ₂	Silicon oxide
SIPOS	Semi-insulating polycrystalline silicon
SRH	Schottky-Read-Hall
STC	Standard test condition
T	Transmittance
TLM	Transmission line model
XPS	X-ray photoelectron spectroscopy

List of Figures

Figure 1 The estimate of finite and renewable planetary energy reserves given in TW/year.....	1
Figure 2 (a). Annual PV module production from 2005 to 2016. (b). Annual PV system installation from 2005 to 2016.	2
Figure 3 A typical J-V curve for a solar cell.....	4
Figure 4 Schematic illustration of (a) radiative recombination, (b) Auger recombination and (c) SRH recombination.....	6
Figure 5 Structures for (a). passivated emitter and rear cell (PERC) and (b). passivated emitter rear locally diffused (PERL) c-Si solar cell.	8
Figure 6 The band diagrams of (a). n-Si with a metal contact (b). n-Si contact with a wide bandgap material and (c). n-Si with conduction band -aligned passivating layer.....	9
Figure 7 Schematic band diagram of poly-Si passivating contacts with n ⁺ poly-Si.	9
Figure 8 Sketch of solar cell with diffused emitter at front and n-type passivated contact at the back. .	10
Figure 9 Sketch of the IBC solar cell.	11
Figure 10 The sketch of the IBC poly-Si passivating contacts solar cell.	13
Figure 11 Schematic structures of the main process steps of poly-Si symmetrical test sample.	14
Figure 12 Schematic structures of the main process steps of front surface passivation symmetrical test sample.....	15
Figure 13 Schematic structures of the main process steps of IBC poly-Si passivating contacts solar cell.	16
Figure 14 R _T versus L graph.	17
Figure 15 Schematic of (a) n-type poly-Si passivating contacts and (b) p-type poly-Si passivating contacts. The blue lines show the case when dopants diffuse too deep into c-Si and red lines show the case when dopants diffuse shallow into c-Si.	21
Figure 16 Phosphorous distributions at poly-Si/c-Si interface at different implantation dose (a) with 75 nm poly-Si and annealing in N ₂ atmosphere at 850 °C for 90 min and (b) with 250 nm poly-Si and annealing in O ₂ atmosphere at 950 °C for 5 min.....	24
Figure 17 The dopant profiles for boron implanted into poly-Si, the implantation dose is 5 × 10 ¹⁵ /cm ² , energy is 5 keV and 950 °C annealing at O ₂ atmosphere.	25
Figure 18 TEM picture of the c-Si/poly-Si interface in scale of (a) 50-nm scale and (b) 5-nm scale.	29
Figure 19 Specific contact resistance of Al/ doped poly-Si/ c-Si contacts before post annealing and after post annealing at 600 °C for 30s.	30
Figure 20 Schematic IBC solar cell with poly-Si passivating contacts (a). no Al ₂ O ₃ at back side (b) Al ₂ O ₃ at back side.	31
Figure 21 Surface passivation quality of phosphorous implanted textured n-FZ Si wafer as a function of the a-Si:H (a) deposition temperature with fixed deposition time of 36s and (b) deposition thickness with fixed deposition temperature of 250°C.	34

Figure 22 Schematic of poly-Si passivating contacts IBC solar cell with optimized front and back passivation layer and tunnel oxide is formed in 67.5% HNO₃ for 1 hour. 35

Figure 23 (a) EQE, 1-R, 1-R-T of cell 3 (b) J-V curve of cell 3. 36

Figure 24 Schematic of poly-Si passivating contacts IBC solar cell with (a) ideal thermal oxide isolation (b) real thermal oxide isolation. 37

Figure 25 EQE curves of solar cells with different a-Si on FSF. 39

Figure 26 The effect of annealing time on (a) V_{oc} (b) FF at 600 °C in N₂ atmosphere. 40

Figure 27 Contact resistivity of Al/a-Si:H/n-type poly-Si and Al/a-Si:H/p-type poly-Si contacts after annealing at 600 °C for 20s. 41

Figure 28 Schematic of the structure of the IBC solar cell with poly-Si passivating contacts with the improved process flow. 45

Figure 29 The relation of H, Si, and N density and refractive index in a-SiN_x:H. 46

List of Tables

Table 1 Passivation of poly-Si layers with different implantation dose.	23
Table 2 Passivation of poly-Si layers with different annealing condition.....	26
Table 3 Passivation of poly-Si passivation structure with different tunnel SiO ₂ formation.	28
Table 4 Performance of poly-Si passivating contacts IBC solar cells.....	31
Table 5 Performance of poly-Si passivating contacts IBC solar cells with optimized front and back passivation and different FSF implantation dose.....	35
Table 6 Performance poly-Si passivating contacts IBC solar cell with real oxide isolation.	37
Table 7 Performance of solar cells respect to the variation of the thickness of a-Si:H passivation layer on FSF.	38
Table 8 Performance of solar cells with different a-Si:H at rear side with 22nm a-Si at front side.	39

1

Introduction

1.1 Background

The fossil energy reserves are declining sharply with the continuous increase of the energy demand. The increase of the fossil fuels usage results in a drastically rise of greenhouse gases emission which leads to climate change. In order to improve the energy consumption situation and reduce the environmental pollution, many countries make a huge effort on shifting from fossil fuel-based energy system to renewable energy system. In 2015, renewable energy in power generation take nearly 3% of global primary energy consumption [1]. Among all kinds of renewable energy resources, solar energy shows the most abundant recoverable energy reverses. Figure 1 illustrates the estimate of finite and renewable planetary energy reserves in 2009 by International Energy Agency (IEA) [2], which shows that the renewable energy, especially solar energy resources, are much more abundant than fossil fuels.

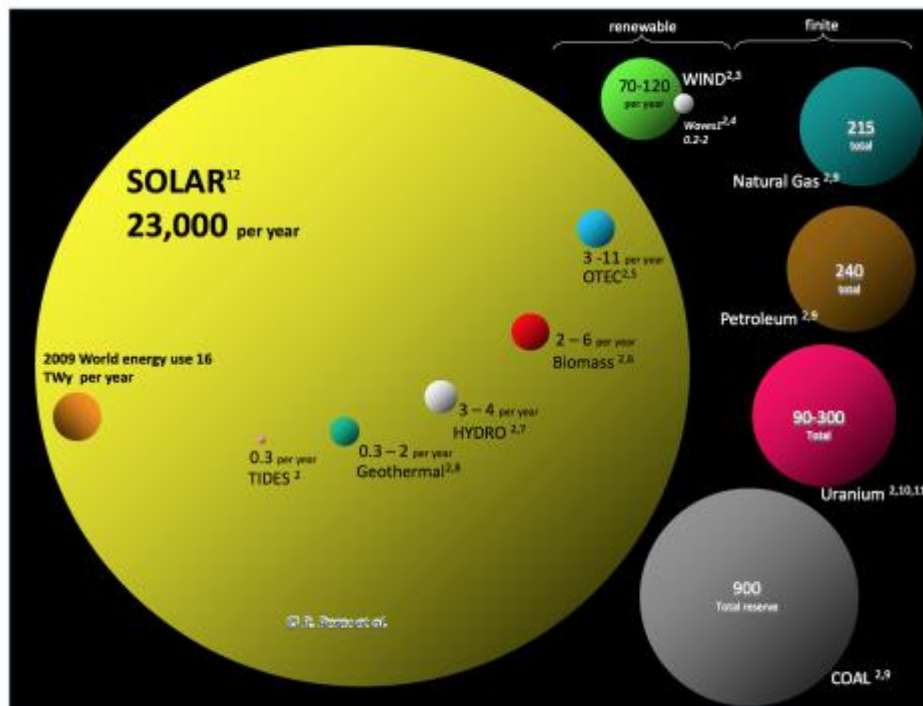


Figure 1 The estimate of finite and renewable planetary energy reserves given in TW/year [2].

To make full use of solar energy, photovoltaic (PV) system is imperative to transfer the solar irradiance to electricity. Figure 2 (a) and (b) shows the annual PV module production and installation from 2005 to 2016. The number of the annual PV module production increased from lower than 5 GW in 2005 to over 70 GW in 2016 for production and the same trend is shown for annual PV installation. The increase in PV production and installation indicates that countries all over the world pay more attention to solar energy development. The Asian countries, especially China and Japan, contributes the most in the increment in PV market in last ten years.

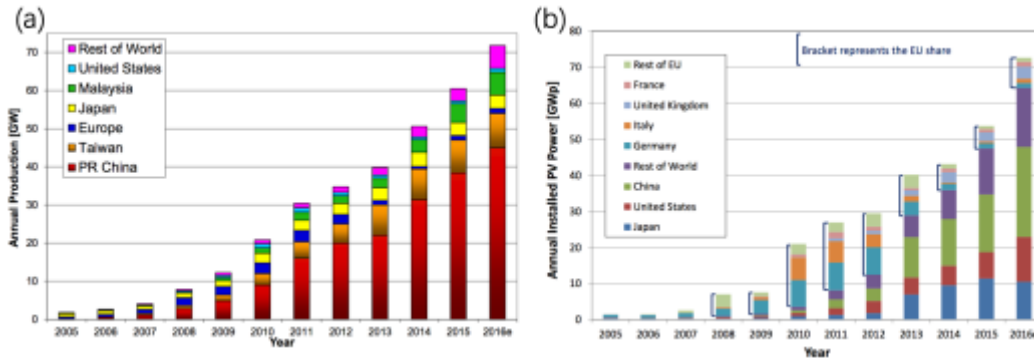


Figure 2 (a). Annual PV module production from 2005 to 2016 [3]. (b). Annual PV system installation from 2005 to 2016 [3].

In this chapter, firstly, the working principle of a solar cell and its characterization are explained. Also, the recombination and passivation mechanisms are presented. Then, several high-efficiency single junction crystalline silicon solar cell concepts are introduced. Finally, the objective and the outline of this thesis are described.

1.2 The basic working principle of a solar cell and characterization

The system of absorbing the solar energy to transfer it to the electricity is called PV systems. The components of a PV system are PV modules, power electronic components and storage devices, it also has electrical interconnections and solar tracking devices. Generally, a PV module consists of solar cells and PV modules forms a PV array. Therefore, solar cells are the main components of a PV system and the main loss also happens in solar cells. First of all, it must be clear that how a solar cell works.

1.2.1 Basic working principle of a solar cell

The working process of a solar cell can be divided into three steps [4]:

- (1). **Generation of charge carriers due to the absorption of photons in the materials that form a junction.**
- (2). **Subsequent separation of the photo-generated charge carriers in the junction.**
- (3). **Collection of the photo-generated charge carriers at the terminals of the junction.**

These three steps represent the basic principle of the photovoltaic effect, which can also be explained that a material generates voltage or electric current under light exposure.

When a photon with the energy higher than the bandgap energy E_G , the electron with the energy lower than valence band E_V can be excited to the conduction band E_C after the absorption of the photon. The

bandgap energy is the energy difference between E_C and E_V and the energy of a photon is given by:

$$E = h\nu \quad (1.1)$$

here h is Planck's constant which is $6.626 \times 10^{-34} \text{ J} \cdot \text{s}$ and ν is the frequency of the light. But when a photon has energy lower than E_G , it will go directly through the semiconductor material without any interaction.

However, photons with enough energy are imperative but not all the story to generate electron-hole (e-h) pairs. The semiconductor can also be divided to direct bandgap material and indirect materials. For direct bandgap materials, a photon with energy higher than bandgap is enough to generate e-h pair. For indirect bandgap material, crystal momentum of the lowest of E_C and highest level of E_V are not the same. To be more specific, when an electron is excited to E_C from E_V , the crystal momentum also need to be changed. This makes the absorption coefficient α of direct bandgap material, such as gallium arsenide (GaAs), is much higher than indirect bandgap material, such as c-Si.

After photons are absorbed and e-h pairs are created, electrons and holes will recombine if no action is taken to separate them. The recombination mechanisms will be introduced in section 1.3. To collect one certain type of the photo-generated carriers, semipermeable membranes are needed and then PN junction is formed. Even though semipermeable membranes are present adjacent to the absorber, charge carriers still have a chance to recombine on their way to the membranes. This requires the absorber thickness smaller than the diffusion length of electrons and holes.

When the charge carriers reach the emitter or back surface field (BSF), they will flow to the external circuit and convert to electric energy. For example, in n-type substrate c-Si solar, holes will be collected in emitter which is highly boron doped region and electrons will be collected in BSF, a highly phosphorus doped region. Electrons will then pass through the external circuit and recombine with holes in emitter.

1.2.2 External Solar cell parameters and external quantum efficiency

The performance of a solar cell can be presented by external parameters which are short circuit current density J_{SC} , open circuit voltage V_{OC} , fill factor FF. These values can be determined by illuminated J-V measurement and conversion efficiency can be calculated from these parameters. The external quantum efficiency (EQE) is also an important parameter that reflects the optical properties of the solar cell.

The **short-circuit current** I_{SC} is the current flow through the solar cell when the voltage across the solar cell is zero, that means the solar cell is short-circuited. As I_{SC} relates to the surface area of the solar cell and that is variable for different solar cells, then the short-circuit current density J_{SC} is used to remove the influence of the area. When the solar cell is measured under standard test condition (STC), J_{SC} is the maximum current that a solar cell can reach. Here, the STC is the temperature of a measured cell at 25°C and it is illuminated by an irradiance of 1000 W/m^2 with air mass 1.5 (AM 1.5) spectrum. When takes no loss in consideration, J_{SC} is equal to J_{ph} . The photo-generated current J_{ph} can be calculated as:

$$J_{ph} = eG(L_N + W + L_P) \quad (1.2)$$

where e is elementary charge, G is generation rate. L_N and L_P are the minority carrier diffusion length for electrons and holes, respectively. W is the width of depletion region. In real solar cells, J_{SC} is smaller than J_{ph} because of the contact resistivity and other non-ideal loss.

The **open-circuit voltage** V_{OC} is the voltage across the solar cell when there is no current flow, in other words, the solar cell is under open-circuit condition. The open-circuit voltage is given as the equation below:

$$V_{OC} = \frac{kT}{e} \ln \left(\frac{J_{ph}}{J_0} + 1 \right) \quad (1.3)$$

here, k is Boltzmann constant and it is equal to $1.38 \times 10^{-23} \text{ J/K}$, and T is temperature in Kelvin. J_0 is the dark saturation current and it depends on the recombination in the solar cell. Therefore, the lower the recombination rate in solar cell, the lower the J_0 . And as a consequence, high V_{OC} can be obtained. Thus, V_{OC} represents the recombination rate in the solar cells.

Fill factor (FF) is the ratio of maximum power can be draw from a solar cell to the product of V_{OC} and J_{SC} . It is determined from J-V measurement and it can be presented as:

$$FF = \frac{V_{mpp} J_{mpp}}{V_{OC} J_{SC}} \quad (1.4)$$

here, V_{mpp} and J_{mpp} are the maximum voltage and current density that a solar cell can deliver. Fill factor depends largely on series resistance (R_s) and shunt resistance (R_{sh}) in a solar cell. In order to have a high FF, the series resistance should be as low as possible and shunt resistance should be as high as possible. The series resistance mainly comes from the bulk resistance of the semiconductor, the resistance of electrodes and the contact resistance at metal semiconductor interface. Leakage across the p-n junction around the edge, crystal defects and pinholes are the sources of shunt resistance.

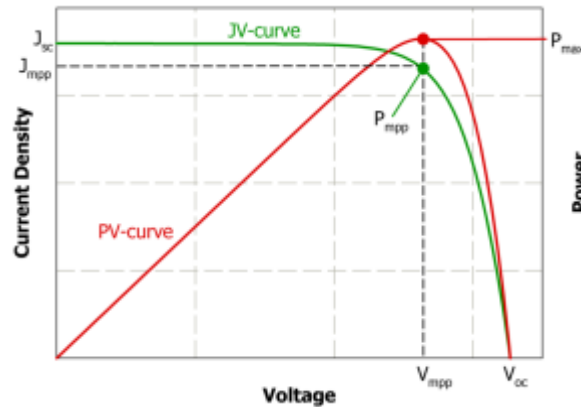


Figure 3 A typical J-V curve for a solar cell [4].

A typical J-V curve of a solar cell is shown in Figure 3. The green curve is measured J-V curve and the red curve is the power delivered by the solar cell. The red point is the maximum power and the green point shows the corresponding voltage and current. Then, the **conversion efficiency** η can be written by J_{SC} , V_{OC} and FF :

$$\eta = \frac{P_{max}}{P_{in}} = \frac{V_{mpp} J_{mpp}}{P_{in}} = \frac{V_{OC} J_{SC} FF}{P_{in}} \quad (1.5)$$

where P_{in} is power of incident light, 1000 W/m^2 under STC. So, once J_{SC} , V_{OC} and FF are determined, the conversion can be calculated.

For a 160 um c-Si wafer based single junction solar cell, the maximum values of J_{SC} , V_{OC} and FF under STC are given below:

- The maximum short-circuit current density is about 44 mA/cm^2 [5].

- b. As the c-Si is an indirect bandgap material, Auger recombination dominates. If only consider auger recombination, the maximum open-circuit voltage is 762 mV [5].
- c. The maximum fill factor given by Green is 89% [6].

Thus, the maximum conversion efficiency of a single junction c-Si solar cell is 29.43% [7].

The **external quantum efficiency (EQE)** is the ratio between collected the electron-hole pairs generated by incident light to number of incident photons. The EQE depends on the wavelength of the light and it is given by:

$$EQE(\lambda_0) = \frac{I_{ph}(\lambda_0)}{e\phi_{ph}(\lambda_0)} \quad (1.6)$$

where I_{ph} is photo-generated current and ϕ_{ph} is incident photon flux to the solar cell which is determined by a calibrated photodiode. EQE is an important parameter that reflects the spectral response and indicates the optical properties of the solar cell. When an EQE is measured under short-circuit condition, that means no bias voltage, the results can be used to determine the short-circuit current density. Equation 1.7 describe the relationship between J_{sc} and EQE. The advantage of determining J_{sc} by EQE is that it does not depend on the spectrum of the incident light compared to J-V measurement AM 1.5 spectrum is imperative. Another advantage is EQE measurement does not rely on the irradiation area. In J-V measurement, the irradiation area must be exactly the same as the solar cell area. Otherwise, the charge carrier generated outside the solar cell may also be collected. However, the accurate solar cell area is not easy to confine when performing the J-V measurement.

1.3 Recombination mechanism & passivation

From the characteristics of the solar cell introduced in the last section, it is easy to find out the way to improve the solar cell performance. To increase the conversion efficiency, one can increase J_{sc} , V_{oc} or FF of the solar cell. In this section, the way to boost V_{oc} is introduced. To increase V_{oc} , the J_0 must be reduced which can be derived from equation 1.3. J_0 is known as dark saturation current density and it is determined by the recombination rate in a semiconductor material. In order to have a high-efficiency solar cell, J_0 should be kept as low as possible. Specifically, the recombination rate should be low.

1.3.1 Recombination mechanisms

The main recombination mechanisms in a semiconductor material are radiative recombination, Auger recombination, and Shockley-Read-Hall (SRH) recombination. For different types of semiconductor, different recombination mechanisms dominate.

First, **radiative recombination**, which is also called direct recombination, mainly happened in direct bandgap material semiconductor, such as GaAs. Figure 4 (a) briefly illustrates the mechanism of radiative recombination. Electrons in conduction band directly recombine with holes in valence band and energy is released in a way of photons. This kind of recombination does not require a change in momentum so it is the dominated recombination mechanism for a direct bandgap material.

Auger recombination plays a dominant role in indirect bandgap material, for example, c-Si. In Auger recombination, electrons in conduction band recombine with holes in valence band like what happens in direct recombination. However, not only energy is released but also momentum must be transferred. The energy and momentum released by recombination are transfer to another electron (hole), and that electron (hole) in conduction (valence) band will be driven to the higher (lower) level of conduction

(valence) band. Later, the excited electron (hole) will go back to the previous energy state again and the released energy will cause lattice vibration and heat in the end. Figure 4 (b) shows the mechanism of Auger recombination.

Shockley-Read-Hall (SRH) recombination is actual dominant recombination for high efficiency solar cells in most case. Within the forbidden bandgap, there are also some energy states which is called trap states. These trap states are caused by impurity atoms or lattice defects in semiconductor lattice. Electrons can be captured by those energy levels, and then recombine with holes that attracted by trapped electrons. Or the trapped electrons fall to the valence band and then recombine like it is shown in Figure 4 (c). The energy released by recombination is dissipated as heat. There is a special case for SRH recombination, which is surface recombination. The dangling bonds at the surface of the semiconductor material can also act as defects and surface recombination is the main loss for some high-efficiency solar cells.

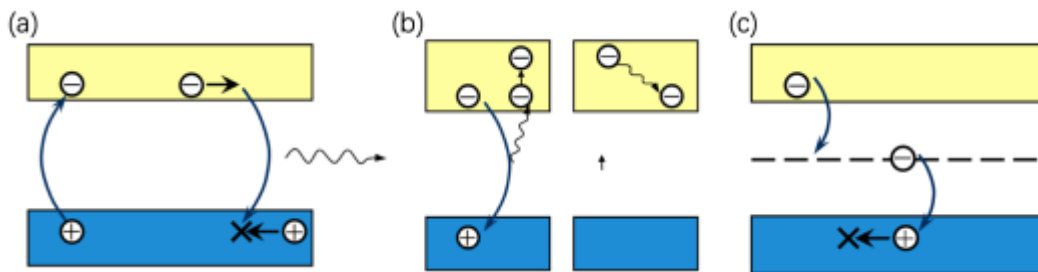


Figure 4 Schematic illustration of (a) radiative recombination, (b) Auger recombination and (c) SRH recombination [4].

1.3.2 Passivation mechanisms

For a high-quality monocrystalline silicon wafer-based solar cell, such as float zone wafer, the bulk recombination can be limited at a very low level. Then, the surface recombination becomes the main mechanism that affects the solar cell performance. In order to reduce the surface recombination velocity, surface passivation is of significance to solar cells. There are two mechanisms of surface passivation which are chemical passivation and field-effect passivation.

Chemical passivation is a way to reduce the interface defects density by depositing a thin layer of insulation material on surface of the semiconductor material. The thin insulation layer will reduce the dangling bond at surface and also provide hydrogenation effect at the most time. The reason for the choice of the insulator is to remain charge carriers inside the semiconductor. Typical chemical passivation layers are silicon oxides (SiO_x), hydrogenated amorphous silicon nitride ($\text{a-SiN}_x\text{:H}$) and hydrogenated amorphous silicon (a-Si:H) [8][9]. SiO_2 can be deposited by plasma enhanced chemical vapor deposition (PECVD) or formed thermally [10][11]. Silicon nitride can also be deposited by PECVD and it can also be used as anti-reflection coating as N-rich SiN_x has refractive index around 2 [10][11][12][13]. Recently, Aluminum oxide (Al_2O_3) deposited by atomic layer deposition (ALD) is developed and used to provide good passivation property to p-type silicon since it has negative charge around $10^{12}/\text{cm}^2$ [10][14][15][16][17].

Another approach to reduce the surface recombination is to reduce the one of the two carriers' concentration by employing highly doped layer, which is known as field-effect passivation. The electric field is set up by highly-doped layer and repels the minority carrier from the highly-doped region. For

example, for an n-type c-Si solar cell, the emitter is a highly boron-doped region, it rejects electrons and only let holes pass through. In this way, the surface recombination reduced significantly. However, for a solar cell with emitter at front side, a too high doping level will cause a poor blue response. This is because high doping comes at the expense of high Auger recombination, so charge carriers generated by blue light in first few nanometers of semiconductor material will recombine via Auger recombination.

1.4 Concepts of high-efficiency c-Si single junction solar cell

To fabricate a high-efficiency solar cell, recombination rate should be kept as low as possible. For c-Si based solar cell, radiative recombination is not the main loss mechanism since c-Si is an indirect bandgap material. The reduction of Auger recombination can only be achieved by means of increasing the wafer resistivity or reduce the wafer thickness. However, the increase of wafer resistivity means the higher lateral current flow resistance and lower FF, thinner c-Si wafer may cause incomplete light absorption. Compare to previous two recombination mechanisms, the reduction of SRH recombination is easier to achieve without the influence of other performance. The low SRH recombination requires both low bulk defects density and good surface passivation. Therefore, wafer-based solar cells always choose monocrystalline wafers which have low bulk defects density. The substrate wafers have n-type and p-type. In the early stage, most high-efficiency solar cells based on p-type c-Si wafers, such as passivated emitter and rear cell (PERC) and passivated emitter rear locally diffused (PERL) c-Si solar cell. This is because the early usage for PV is on space application, for example, providing power for satellites and space exploration robots. This working environment requires solar cells a high endurance with high-energy particles in space, so p-type c-Si is chosen. Later, with the industrialize of PV, many research groups turn to n-type c-Si. The advantages of n-type c-Si compared to p-type c-Si are that n-type c-Si has higher endurance to most metallic impurities, such as iron [18]. Meanwhile, n-type c-Si does not suffer from light induced degradation (LID) as it mainly induced by defects caused by boron and interstitial oxygen in p-type CZ wafers or p-type poly-Si wafers [19].

In this section, homo-junction solar cells and solar cells with carrier selective contacts are introduced. The homo-junction is formed by dopant diffusion into c-Si, therefore the p-n junction is formed by the same material. For example, both PERC and PERL solar cell are homo-junction solar cells. Solar cells with carrier selective passivating contacts always have a p-n junction formed with two different materials, such as heterojunction solar cells and solar cells with poly-Si passivating contacts.

1.4.1 Homo-junction solar cells

In 1989, PERC structure was demonstrated in UNSW with the efficiency of 22.8% [20], and 1999 the PERL solar cell with the efficiency of 24.7% was achieved again in the same research group [21]. The structure of PERC and PERL solar cells are shown in Figure 5. Both PERC and PERL solar cells are homo-junction solar cells, emitter is formed by phosphorus diffusion and it is highly doped near metal to reduce the recombination velocity at the metal-semiconductor interface. The high recombination rate at c-Si and metal interface requires a minimal metal semiconductor contact area at rear side, and as a consequence, a point contact design is used. The difference between PERC and PERL solar cells are that PERL solar cell also has a highly-doped boron diffusion region at rear side, this reduces the recombination and increase the V_{oc} . The double antireflection coating at front side minimized the reflection and gives rise to J_{sc} .

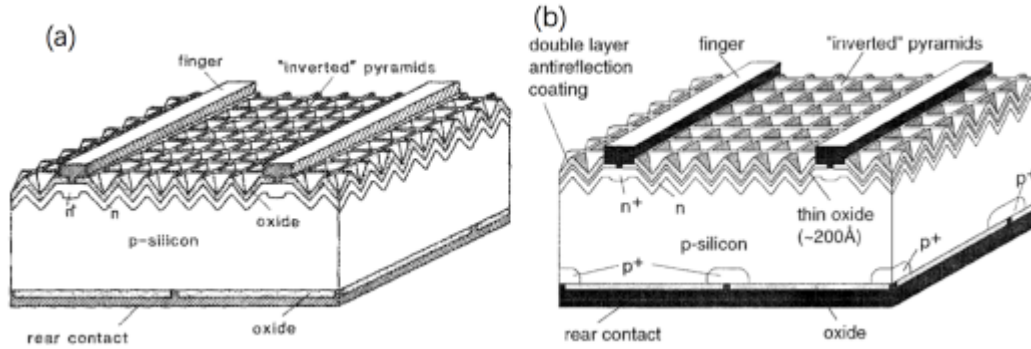


Figure 5 Structures for (a). passivated emitter and rear cell (PERC) [20] and (b). passivated emitter rear locally diffused (PERL) c-Si solar cell [21].

1.4.2 Solar cells with carrier selective passivating contacts

Although PERL solar cells use point contacts at rear side, the recombination at metal-semiconductor interface still plays a significant role in solar cell performance. It can be seen from the V_{oc} value which is 706 mV which has a large gap to maximum V_{oc} , 762 mV. The high recombination rate at the metal-semiconductor interface is because of the high interface states density in the forbidden c-Si bandgap of the metal. These energy states act as trap states in SRH recombination and induce a large J_0 value. Figure 6 (a) illustrates the band diagram of the metal-semiconductor contact [22]. In order to increase the open circuit voltage, the recombination rate at n-Si surface must be decreased. A dielectric or wide bandgap materials are used to passivate the defects at the n-Si surface which called chemical passivation, such as a-Si:H, SiO_2 or Al_2O_3 , the band diagram is shown in Figure 6 (b) [22]. Although the dangling bonds at n-Si surface are passivated, there is no selectivity for charge carriers. That means no photo-generated carriers can pass through the passivating layer, then it can be employed for neither emitter or BSF.

There are several ways to make the contact selective for one certain carrier, the way used in homo-junction solar cells is inserting a highly-doped region between c-Si and the metal-semiconductor contact, so the conductivity of one certain carrier is reduced and the carrier selective function is realized. For example, the p^+ region near the metal contact increase the distance between quasi-Fermi level for electrons and conduction band which causes a conduction band offset, then the selectivity for holes is realized. The drawback of this approach is that it increases Auger recombination in highly doped region as it is mentioned above.

One way to avoid this disadvantage is to deposit a wide bandgap material with small conduction band offset. Hydrogenated amorphous silicon with highly dopant concentration is such a material that provides excellent passivation properties and can realize carrier selectivity, and Figure 6 (c) briefly introduces the band diagram of this structure. A good example is the heterojunction solar cell (HJT) fabricated by Panasonic, and the highest V_{oc} is 750 mV with the efficiency of 24.7% [23]. However, the a-Si in the HJT cell limit the process temperature up to 250 °C, so the TCO deposition and metallization steps need to be carefully designed to avoid the release of the hydrogen from a-Si [24]. Meanwhile, the a-Si will induce a high parasitic absorption at the front side and ITO is a very expensive material [22].

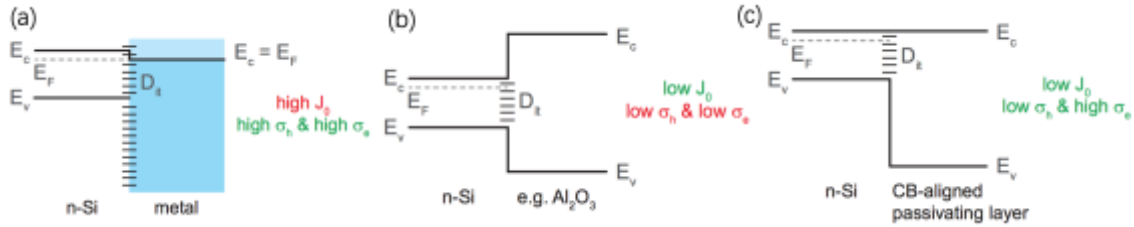


Figure 6 The band diagrams of (a). n-Si with a metal contact (b). n-Si contact with a wide bandgap material and (c). n-Si with conduction band -aligned passivating layer [22].

Another way is to achieve a carrier selective passivating contact by using poly-Si passivating contacts. The band diagram shown in Figure 7 illustrates that the poly-Si passivating contacts based on two main aspects, an ultra-thin SiO_2 layer and a heavily doped poly-Si layer. This structure was first used in the bipolar transistor [25], and then tested by Yablonoivitch et al. that it has 720 mV V_{OC} with n^+ -SIPOS/thin SiO_2 /p-type c-Si/thin SiO_2 / n^+ -SIPOS structure [26].

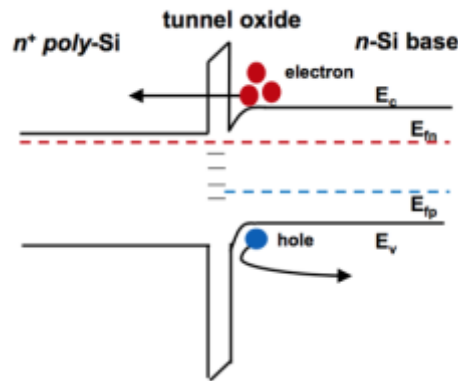


Figure 7 Schematic band diagram of poly-Si passivating contacts with n^+ poly-Si [27].

The oxide layer is always thinner than 2 nm, it gives a good chemical passivation, while majority charge carriers can still go through this thin oxide layer by tunneling. The highly-doped poly-Si enables the band bending in c-Si, which reduces the conductivity of one type of charge carriers and increases the conductivity of another type of charge carriers. Therefore, carrier selectivity is realized in this way [28]. For example, the n^+ poly-Si in Figure 7 provides a band bending at c-Si/poly-Si interface which allows electrons to tunnel through and repels holes as the existence of valence band offset. Meanwhile, it can be assumed that there are no states in the forbidden gap of poly-Si, so holes will not tunnel through. Poly-Si has higher thermal stability than a-Si, therefore, it allows high-temperature process, such as high temperature metallization fire-through. According to the research by R. Peibst et al., the energy barrier difference between electrons and holes provides by tunnel oxide also contributes to the carrier selectivity [29]. It is 4.5 eV for holes to tunnel while the value for electrons is 3.2 eV [29].

By using the poly-Si passivating contacts at the rear side, 25.1% efficiency was achieved in 2015 [30]. The front emitter of this record cell is passivated by Al_2O_3 and SiN_x as anti-reflection coating (ARC), the emitter under metal contact is heavily-doped by boron atoms to realize carrier selectivity and reduce recombination at interface, the structure is shown in Figure 8.

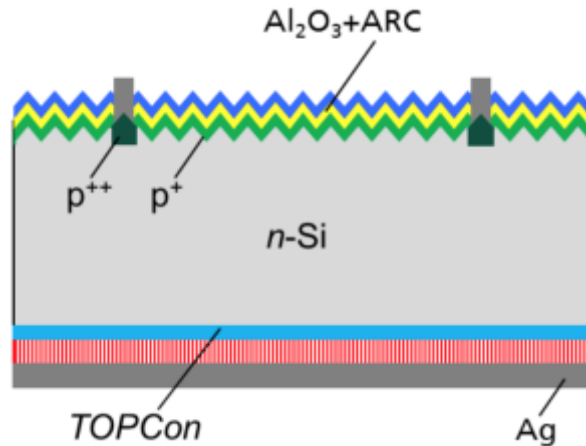


Figure 8 Sketch of solar cell with diffused emitter at front and n-type passivated contact at the back [30].

The charge carrier transport mechanism through tunnel oxide is not completely clear yet. There is another model explains that the current flow is based on the pinholes on the oxide which is formed during thermal annealing [29]. The physical properties of SiO_2 largely depend on the growth method and the way it affects the performance on passivation is still under discussion.

1.4.3 The interdigitated back contact solar cell

All solar cells mentioned above have both front and rear metal contacts, therefore the shading caused by metal contacts at front side induces optical loss. To avoid this shading loss, the interdigitated back contact (IBC) solar cells is developed. Figure 9 shows the sketch of an IBC solar cell, where all the metal contacts are on the back side. The n^+ front diffusion region is called front surface field (FSF), which enhances the UV response of the solar cell in the way of decrease front surface recombination via field-effect passivation. However, the highly-doped region always suffers from the increase of Auger recombination, this is also the case for FSF, so the dopants within FSF should be kept in a shallow region. All the metal can be designed as wide as possible at the rear side to reduce the series resistance caused by metal and act as the back reflector.

Combine the IBC and HJT concepts, a world record efficiency 25.6% is reached in 2014 [31]. Recently, Japanese company Keneka Corp. successfully fabricate a HJT-IBC solar cell with efficiency of 26.6% [32], which is very close to the maximal efficiency 29.4%. Meanwhile, IBC can also combine with poly-Si passivating contacts. ISFH demonstrated a solar cell with such a structure called polysilicon on oxide (POLO) junction with back junction back contact (BJBC) solar cell with the efficiency of 24.25% [33].

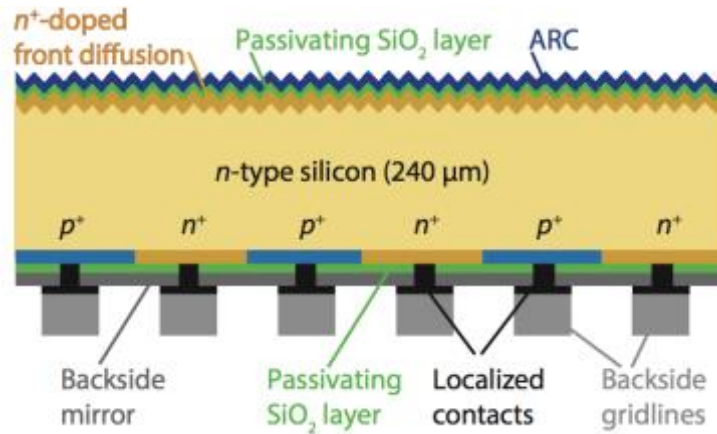


Figure 9 Sketch of the IBC solar cell [4].

1.5 Objective and thesis outline

The objective of this thesis is to improve the efficiency of IBC solar cells with poly-Si passivating contacts based on the process flow developed in the PVMD group. The main research questions are: how to improve passivation performance of front surface and poly-Si passivating contacts, and their influence on the solar cell performance, which are investigated with the following can four aspects.

1. Field-effect passivation optimization on BSF and emitter at rear side of the solar cell;
2. Tunnel oxide optimization of poly-Si passivating contacts;
3. Front surface field and its passivation layer optimization;
4. Solar cells fabrication with optimized structures.

Chapter 2 describes the experiment details on the symmetrical test samples fabrication and the solar cells process. The equipment used for process and measurement are also introduced in this chapter. In chapter 3, the poly-Si passivating contacts for BSF and emitter are improved by the optimization of implantation dose on BSF and emitter, their annealing condition, and the optimization of tunnel oxide. The improvements in performance of solar cells with the above-mentioned optimization are also presented. In chapter 4, passivation on front surface is studied by optimizing the implantation dose and their passivation layers. The deposition temperature and thickness of a-Si:H passivation layers are investigated. Solar cells with the optimized FSF implantation dose and passivation layer are reported and discussed. Chapter 5 contains the conclusions of all the experiments and recommendations for further research.

2

Experiment

2.1 Introduction

In this chapter, the main experiments conducted in this thesis are explained in detail. Firstly, let us take a close look at the structure of the IBC poly-Si passivating contacts solar cells studied in this work (see Figure 10). The substrate is n-type float zone (FZ) monocrystalline silicon wafer, which has fewer bulk defects compare to Czochralski wafer. The n^{++} and p^{++} poly-Si at back side are BSF and emitter, separately. Between poly-Si and n-FZ substrate, there is an ultra-thin layer of SiO_2 , <2 nm, which has the function of chemical passivation on c-Si as well as tunneling of majority carriers. The dopants in poly-Si are inserted by ion-implantation and followed by high-temperature annealing to activate these dopants. The function of FSF is to reduce the surface recombination as it forms an electric field which rejects the minority carriers at front surface from recombination. Since light with short wavelength has larger absorption coefficient, most of UV light will be absorbed near the surface. The FSF can enhance the stability of passivation performance for short wavelength light. The passivation layers on both the front side and the rear side of the cell are to reduce the surface recombination and gives hydrogenation to the poly-Si/c-Si interfaces. SiN_x layer on the textured front surface acts as an anti-reflection coating to enhance light absorption.

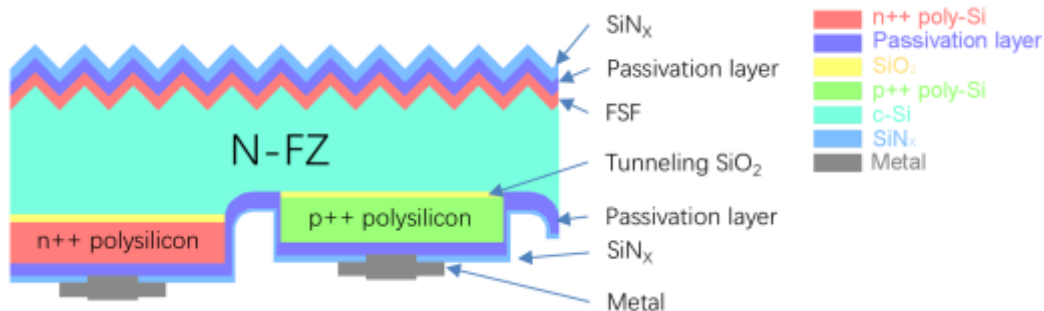


Figure 10 The sketch of the IBC poly-Si passivating contacts solar cell.

The improvement of the IBC poly-Si passivating contacts solar cells performance can be taken in several aspects. Firstly, at the rear side, the poly-Si passivating contacts can be further improved. This includes the optimization of implantation dose in poly-Si as BSF and emitter, the annealing conditions after ion-implantation, and the formation of tunnel oxide. For the metal-semiconductor contact, a thin passivation layer can be implemented between metal and poly-Si contacts to reduce the interface state density. Then, on the front side of the solar cell, the implantation dose on FSF can be changed to reduce Auger recombination and the passivation can be improved in combination with the passivation layer at surface. To optimize these structures, symmetrical tests are made to verify the properties of different

layers.

2.2 Poly-Si passivating contacts

The doped poly-Si layers at back side play roles of emitter and BSF, therefore numerous variables can be changed, such as the thickness of poly-Si and deposition method of poly-Si. In this thesis, only three aspects are optimized regarding of poly-Si passivating contacts, which are **the formation of tunnel SiO₂**, **implantation dose in poly-Si** and **annealing steps**. All these three optimizations are based on the same symmetrical test structure, which means both sides of samples are symmetrically processed and can be regarded as the same. The main fabrication steps are shown in Figure 11.

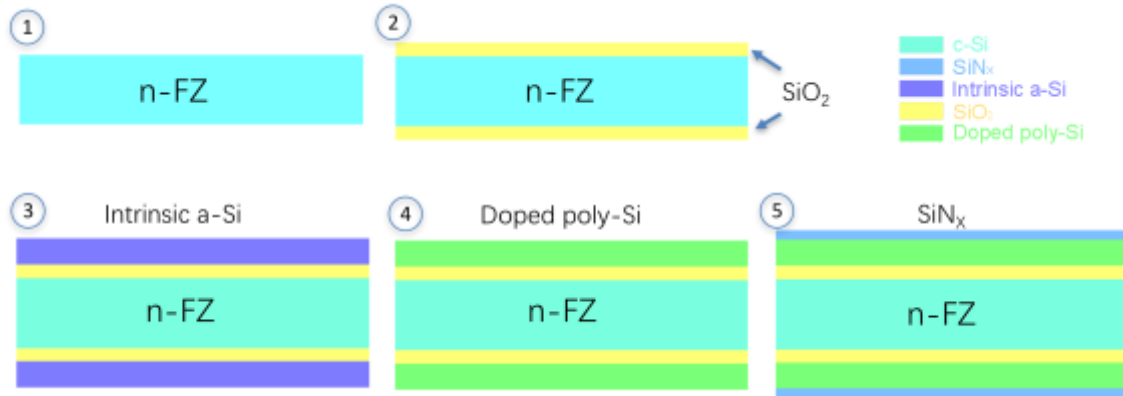


Figure 11 Schematic structures of the main process steps of poly-Si symmetrical test sample.

The process starts from the <100> oriented, 1~5 Ω cm, 285-μm thick, double-sided polished FZ wafers, the native oxide on surface is first removed by a four-minute immersion in 0.55% HF solution. Then, the tunnel SiO₂ is formed by nitric acid oxidation of silicon. The concentration and temperature of HNO₃, and the immersion time are important for the formation of this tunnel SiO₂ and it will be discussed in chapter 3. The next step is the deposition of intrinsic amorphous silicon by low pressure chemical vapor deposition (LPCVD). LPCVD uses high temperature to drive reactions on substrates in the quartz tube, the low pressure is to decrease unwanted gas phase reactions. Steps 4 in Figure 11 shows the structure of samples after ion implantation and annealing. A certain amount ions are accelerated by an electrical field and then inserted into a-Si, the number of ions per area is called dose. The energetic collision caused by high-speed ions with silicon atoms damages the crystal structure and produces defects in silicon. Therefore, annealing is indispensable to recover defects, activate and drive dopants deeper into a-Si. Another important function of annealing is to poly-crystallize the a-Si, this happens when the annealing temperature is higher than 900 °C. The last step is the deposition of SiN_x via PECVD, where PECVD is a chemical vapor deposition technique that use plasma to initiate chemical reactions at relatively low temperature. As the forming gas of SiN_x during deposition are silane (SiH₄) and ammonia (NH₃) both contain abundant hydrogen atoms which can also be used for hydrogenation.

2.3 Front surface passivation

Symmetrical test can also be used to examine the front surface passivation quality with structure depicted in Figure 12. The process also starts from <100> oriented, 1~5 Ω cm, 285-μm thick, double-

sided polished FZ wafers. The wafer is randomly textured on both side to ensure it has the same structure as the real solar cells. Then, the front surface field is formed by phosphorous implanted into the textured c-Si surface and followed by high temperature annealing. After ion implantation, defects density in c-Si surface increases and a passivation layer is needed to be deposited on c-Si to reduce the surface recombination rate. The last step is the deposition of anti-reflection coating, which is SiN_x , to decrease reflection. The thickness of SiN_x at front surface is around 75 nm based on the destructive interference and the characteristic of AM 1.5.

In this thesis, variables changed to enhance passivation within this structure are the property of FSF, the material of passivation layer and its deposition properties.

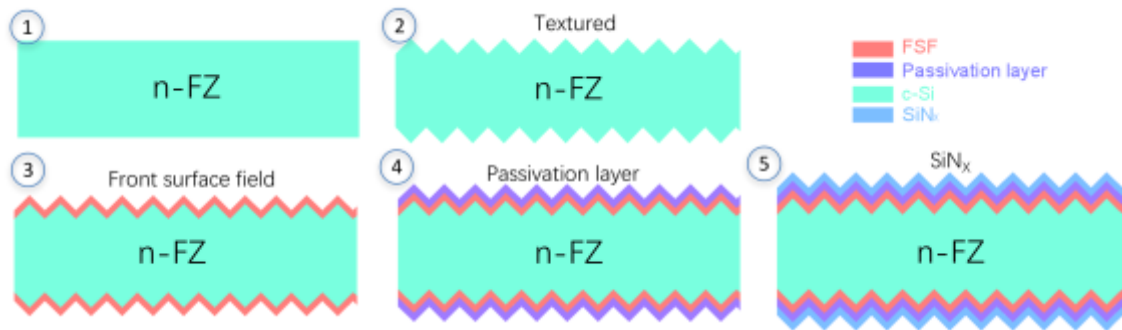


Figure 12 Schematic structures of the main process steps of front surface passivation symmetrical test sample.

2.4 Solar cell fabrication

The main steps of fabricating IBC poly-Si passivating contacts solar cells are shown in Figure 13. The process originates from the self-aligned process for c-Si homo-junction IBC solar cells proposed by Andrea Ingenito in our group [34].

The IBC poly-Si passivating contacts solar cells are based on monocrystalline wafers, therefore, n-type FZ wafers are chosen to ensure a low bulk defect density. Wafers are first dipped into 0.55% HF solution for 4 minutes to remove the native oxide. There are two different ways for the formation of wet chemical oxide. One is the called standard cleaning in cleanroom 100 Else Kooi Laboratory (EKL) in TU Delft. It can be divided into two sub-steps: ten-minute immersion in 99%, room temperature HNO_3 and followed by five-minute rinsing in deionized (DI) water, then ten-minute immersion in 67.5%, 110 °C HNO_3 and followed by five-minute rinsing in DI water as well. The thickness of silicon oxide is 1.5 nm according to previous transmission electron microscopy picture [10]. Another method is to immerse native-oxide-removal n-type FZ wafers into 67.5% HNO_3 for 1h, which gives a stable tunnel SiO_2 with excellent passivation performance.

After the formation of tunnel SiO_2 , sample structure is shown in Figure 13 (1). Then, a 250-nm intrinsic a-Si is deposited on both sides of wafers by LPCVD at 580 °C and followed by one-hour annealing at 600 °C for the stress release as it is described in Figure 13 (2). In order to obtain BSF, intrinsic a-Si is doped by phosphorous atoms via ion implantation. In the next step, a PECVD SiN_x layer is deposited on LPCVD a-Si at back side to prevent the contact with another LPCVD a-Si layer deposited in later steps. Afterward, the SiN_x layer is patterned by photolithography, the BSF area is covered by photoresist which is used as a barrier to prevent etching. So, in the following steps, the unshielded SiN_x at back side is

etched by the buffered HF solution. Later, the unshielded a-Si at rear side is etched away together with tunnel SiO_2 and a very thin layer of c-Si below. All the a-Si at front side, as well as the tunnel SiO_2 , are removed while etching a-Si at back side due to the non-protection as it depicts in Figure 13 (3).

For IBC solar cell, both emitter and BSF are on the back side. Defining the area of BSF is not enough and the following steps are the emitter patterning. Therefore, the tunnel SiO_2 layer is formed again using nitric acid, after which the intrinsic LPCVD a-Si layer deposition happens on both sides of the wafer. The structure is illustrated in Figure 13 (4) till this step. Subsequently, LPCVD a-Si is doped by boron implantation and a PECVD SiN_x layer is deposited on a-Si on the back side. Later, the emitter area is defined by photolithography and SiN_x and a-Si on BSF are etched away. Up to this point, patterning of BSF and emitter is finished, see Figure 13 (5).

In the next stage, the front side of the wafer is processed. During the texturing of the front surface, SiN_x plays a role of protecting the back side from being textured (see Figure 13 (6)). There are two annealing steps, one is before the formation of FSF, which is to activate dopants and poly-crystallize a-Si in BSF and emitter. And after the phosphorous implantation on the textured front side, wafers are annealed at high temperature to activate dopants in FSF and recover defects (Figure 13 (7)). Then, passivation layer and PECVD SiN_x are deposited on both FSF and back side shown in Figure 13 (8). And the final steps are open the SiN_x at back side by photolithography, metallization and lift-off. Figure 13 (9) depicts the sectional view of the complete solar cells.

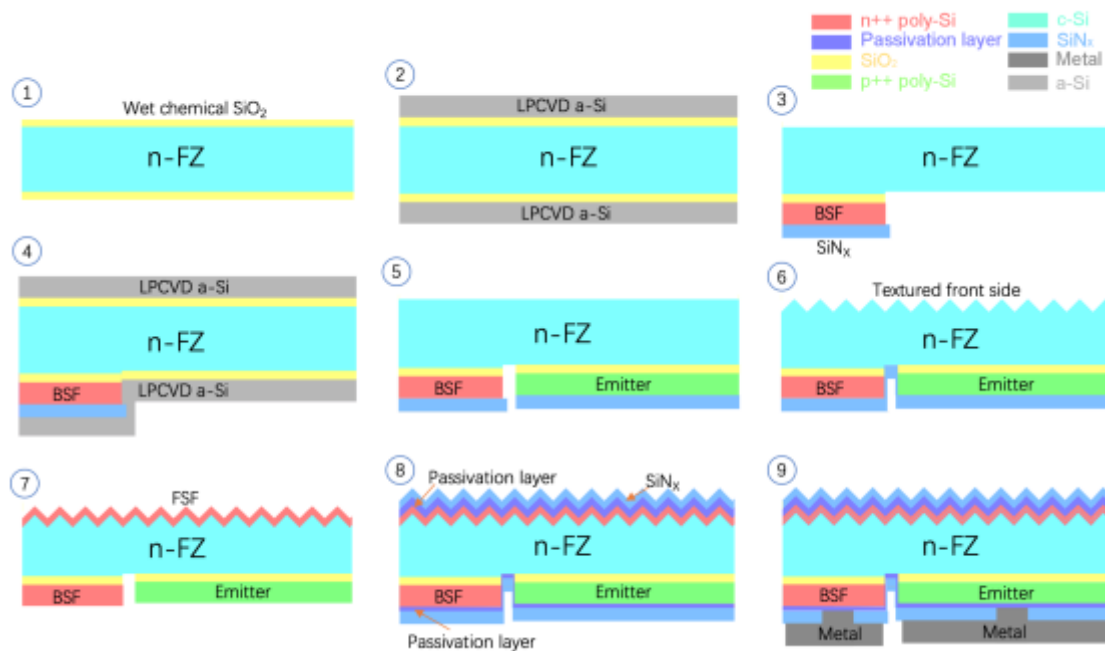


Figure 13 Schematic structures of the main process steps of IBC poly-Si passivating contacts solar cell.

2.5 Measurement equipment

2.5.1 Dark I-V measurement

Dark current-voltage measurement (I-V) measurement is used to determine the electrical performance of a solar cell, such as shunt resistance, series resistance, ideality factor and so on. In this thesis, a

Keithley 6517A electrometer is used to measure the current under a certain voltage range and then the series resistance can be obtained from the fitted curve if all the contacts are ohmic contact.

In fact, the dark I-V measurement in this work is carried out for measuring the contact resistance between different layer by means of transmission line model (TLM) measurements. The TLM measurements is a method to determine the contact resistance between a metal and a semiconductor. The metal bars on samples for TLM measurements are distributed on semiconductor with varying distance between every two neighboring metal bars which is shown in Figure 14. Dark I-V measurement are carried out for every two neighboring metal bars and the measurement resistance is the total resistance which can be represented by:

$$R_T = 2R_M + 2R_C + R_{Semi} \quad (2.1)$$

where R_M is the metal resistance, R_C is the contact resistance between metal and semiconductor, R_{Semi} is the semiconductor resistance. The metal resistance is small compared to contact resistance and semiconductor resistance so that it can be neglected [35]. The semiconductor resistance can be written as:

$$R_{Semi} = R_S \times \frac{L}{W} \quad (2.2)$$

W is the width of the metal bar and L is the distance between two measuring metal bars, R_S is the sheet resistance with the unit of Ω/\square . Thus, the total resistance is:

$$R_T = 2R_C + R_{Semi} = 2R_C + R_S \times \frac{L}{W} \quad (2.3)$$

Based on equation 2.3, the graph of R_T versus L can be plotted (see Figure 14) and contact resistance is obtained from graph.

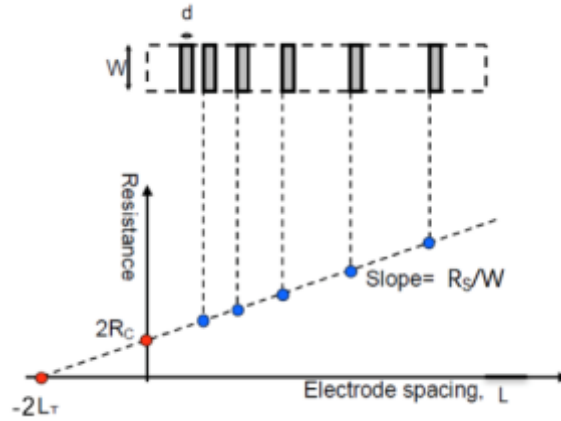


Figure 14 R_T versus L graph.

2.5.2 Photo-conductance lifetime measurement

When testing the properties of a symmetrical sample, the photo-conductance lifetime measurement is critical to examine the performance. Not only the **effective minority lifetime** τ_{eff} , but also the **implied V_{OC}** and **dark saturation current density J_0** can be obtained from this measurement. These values give an indication of the quality of FSF passivation and poly-Si passivation. During measurements, samples are placed under a flash lamp and the minority carrier lifetime is derived from the photo-

conductance decay curve [36]. The photo-conductivity is measured by an eddy-current conductance sensor under the sample after a short light-pulse of the flash lamp and it does not require the direct contact of the sensor and the measured samples. In this work, a WTC-120 of Sinton Consulting Inc. consists of a flash lamp and an eddy-current conductance sensor is used.

The minority carrier recombination happens in both bulk and surface, the effective minority lifetime τ_{eff} is expressed based on recombination mechanism:

$$\frac{1}{\tau_{\text{eff}}} = \frac{1}{\tau_{\text{bulk}}} + \frac{1}{\tau_{\text{surface}}} = \left(\frac{1}{\tau_{\text{rad}}} + \frac{1}{\tau_{\text{Auger}}} + \frac{1}{\tau_{\text{SRH}}} \right) + \frac{1}{\tau_{\text{surface}}} \quad (2.4)$$

where τ_{bulk} , τ_{surface} , τ_{rad} , τ_{Auger} , τ_{SRH} , are minority carrier lifetime regarding to bulk, surface, radiative, Auger and SRH recombination, separately. For devices with short τ_{eff} , a quasi-steady state photo-conductance (QSSPC) method is used. In QSSPC method, the τ_{eff} is measured under quasi-steady state illumination, which means that generation rate and recombination rate equals. This method allows to measure very short lifetime and the detection limit can be as low as 3 ns if the irradiance is increased to 1000 suns [36]. The equation is described below where Δn is excess carrier density and G is carrier generation rate.

$$\tau_{\text{eff}} = \frac{\Delta n}{G} \quad (2.5)$$

For high lifetime measurements, a steady state is not prerequisite. The effective minority carrier lifetime can be derived from the decay of photo-conductance after a shorter light flash than QSS mode. This method is called transient mode where τ_{eff} is calculated from the equation below, the minus comes from the negative trend of the change of minority carrier density.

$$\tau_{\text{eff}} = \frac{-\Delta n}{\frac{d\Delta n}{dt}} \quad (2.6)$$

The implied V_{OC} can also be determined from the change in carrier concentration [37]. Since it is measured under the open-circuit condition, it does not take metal contact loss into consideration. It is derived from equation 2.7, where kT/q is the thermal voltage, N_A is doping concentration, Δn is the excess carrier concentration and n_i is the intrinsic carrier concentration of the semiconductor material. Meanwhile, the dark saturation current density J_0 can also be measured which equals to recombination current density in thermal equilibrium. It is a very important that indicates the quality of surface passivation.

$$iV_{\text{OC}} = \frac{kT}{q} \ln \left(\frac{(N_A + \Delta n)\Delta n}{n_i^2} + 1 \right) \quad (2.7)$$

2.5.3 External quantum efficiency measurement

The EQE measurement gives the spectral response of a solar cell at different wavelength as well as the value of J_{SC} which provides information for improvements of the device. The EQE measurement in PVMD group is carried out with a home-build setup. The light comes from a xenon gas discharge lamp and the light frequency is modified by a chopper. Then, when light with certain frequency pass by the monochromator, a certain wavelength is allowed to pass through and irradiate to the solar cell. The measured solar cell connects with two probes to measure the photo-generated current. The xenon lamp generates light with the wavelength in the range of 200 to 2500 nm. For silicon based solar cell, the measurement range is from 300 to 1200 nm with the step of 10 nm. Before measurement, calibration is needed with a reference diode which is calibrated at Fraunhofer Institute for Solar Energy

(ISE) Systems. Bias light and bias voltage can be also performed, where bias light is used to measure the response of multi-junction solar cells.

2.5.4 Current density-voltage measurement

In principle, the current-voltage measurement should be performed under standard test condition. The requirement of 25 °C and intensity of 1000 W/m² is not difficult to achieve. However, the spectrum AM 1.5 can only be simulated by an artificial light source which always has slightly deviation. In this work, the solar cell is measured with a Class AAA Wacom WXS-156S solar simulator. All the external solar cell parameters can be obtained from this measurement as well as series resistance and shunt resistance. During measurement, the bias voltage sweeps from one value to another and the photo-generated current is collected to find out the maximum power point thence gives the values of all the main solar cell characteristics. The reference cell is also calibrated at ISE.

3

Optimization of poly-Si passivating contacts

The passivation of poly-Si passivating contacts to c-Si surface consists of the field-effect passivation from the emitter and BSF, and chemical passivation of tunnel SiO_2 . As both emitter and BSF are ion-implanted poly-Si, the ion-implantation dose and annealing condition are of significance to the passivation performance from the field-effect passivation point of view. For tunnel oxide, which can be formed in different ways, in this thesis, only wet chemical oxide formed by HNO_3 is used, which is also called as Nitric Acid Oxidation of Silicon (NAOS). The optimization of poly-Si passivation is performed in three aspects: ion-implantation dose on emitter and BSF, discussed in section 3.1, and their annealing condition discussed in section 3.2, and the concentration of nitric acid and the immersion time of the NAOS process for the formation of tunnel SiO_2 , which will be discussed in section 3.3.

3.1 Optimization of implantation dose

The dopants distribution at the poly-Si/c-Si interface affects passivation performance to a large extent, and it is influenced by two factors: implantation dose and annealing condition. The influence of dopants distribution on band bending is shown in Figure 15.

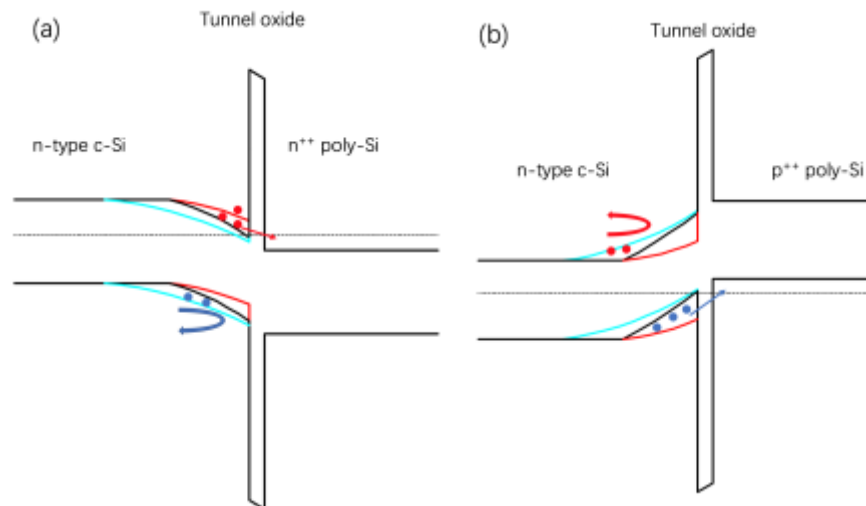


Figure 15 Schematic of (a) n-type poly-Si passivating contacts and (b) p-type poly-Si passivating contacts. The blue lines show the case when dopants diffuse too deep into c-Si and red lines show the case when dopants diffuse shallowly into c-Si.

For n-type poly-Si passivating contacts in Figure 15 (a), dopants in c-Si near interface cause a strong band bending which makes the c-Si surface more n-type and induces electrons accumulation. These majority carriers, electrons, can tunnel through the ultra-thin SiO_2 and minority carrier holes will be

rejected. An ideal dopants distribution can induce the band bending as the black lines show. The conduction band of c-Si at interface is almost the same height as that of n-type poly-Si which promise a good tunneling of electrons as well as strong rejection force for holes. When ion-implantation dose is smaller than optimal value, dopants diffuse too shallow into c-Si and leads to weak electric field for holes and result in a poor passivation as red curves shown. A too high dose leads to deep dopants in c-Si, as it is shown by blue curves, which cause a weak band bending at interface and high Auger recombination in c-Si. For p-type poly-Si passivating contacts, the band diagrams are depicted in Figure 15 (b), and the effect of ion-implantation dose on passivation quality is the same as that of n-type contacts. Thus, proper ion-implantation doses in poly-Si for the formation of emitter and BSF are essential for photo-generated carrier collection and passivation.

In this section, different implantation doses for phosphorous and boron in poly-Si are tested with symmetric test structure, and then photo-conductance lifetime measurements are carried out to determine the passivation quality for poly-Si passivating contacts. Samples for implantation dose test have structures shown in Figure 11, the tunnel oxide is formed via standard cleaning process in Else Kooi Laboratory. It is a two-step cleaning: a ten-minute immersion in 99%, room temperature HNO_3 plus a five-minute rinsing in DI water, then a ten-minute immersion in 67.5%, 110 °C HNO_3 and followed by a five-minute rinsing in DI water again. The thickness of tunnel SiO_2 is 1.5 nm and it is measured by TEM which has already mentioned in section 2.2. The same tunnel oxide for all samples in the same run promises the same chemical passivation for all test samples, therefore the variable that influences the passivation property is only field-effect passivation. The thickness of LPCVD a-Si is 250 nm with around 5% crystallinity which is checked by Raman measurement [10]. The implantation dose for phosphorous varies from $2 \times 10^{15}/\text{cm}^2$ to $1 \times 10^{16}/\text{cm}^2$ and for boron it is $2 \times 10^{15}/\text{cm}^2$ to $6 \times 10^{15}/\text{cm}^2$, the change of implantation dose is to check the effect on field-effect passivation. After ion-implantation, an annealing step is performed in oxygen atmosphere at 950 °C for 5 minutes and the LPCVD a-Si is poly-crystallized with a Raman crystallinity fraction of more than 90% [10]. Before the photo-conductance lifetime measurement, both sides of samples are deposited by thin layers of PECVD SiN_x . The results of both p-implanted and b-implanted passivating contacts are shown in Table 1.

Table 1 Passivation of poly-Si layers with different implantation dose.

Sample	Dopant	Implantation		Passivation		
		Dose [$\times 10^{15}/\text{cm}^2$]	Energy [keV]	Lifetime [us]	J_0 [fA/cm ²]	i-V _{oc} [mV]
1	P	2	20	4133	8.0	719
2	P	3	20	5350	8.0	721
3	P	4	20	7079	7.5	722
4	P	5	20	4140	12.5	713
5	P	6	20	2004	25.0	698
6	P	7	20	1235	37.0	687
7	P	8	20	809	50.0	676
8	P	9	20	611	68.0	668
9	P	10	20	495	76.0	663
10	B	2	5	461	15.0	676
11	B	3	5	546	18.0	679
12	B	4	5	1383	16.0	698
13	B	5	5	555	37.0	674

The only variable in Table 1 for samples with the same dopant is the implantation dose. It is obvious that the best passivation performance happens when implantation dose is $4 \times 10^{15}/\text{cm}^2$ for both phosphorous and boron. The lifetime for n-type poly-Si passivating contacts is about 7 ms with implied V_{oc} at 722 mV, the J_0 is as low as 7.5 fA/cm². For p-type, they are 1.3 ms, 698 mV and 16 fA/cm², separately. Any dose higher or lower than this value shows poorer passivation performance.

The mechanism behind this phenomenon is the that the passivation of poly-Si to c-Si surface is dominated by the field-effect passivation due to the band bending at the interface via a heavily doped poly-Si layer [10][38][39]. For n-type sample with implantation dose at $4 \times 10^{15}/\text{cm}^2$, the phosphorous concentration in poly-Si layer after annealing is around $1 \times 10^{20}/\text{cm}^3$, which means that the poly-Si layer is degenerated doped and the Fermi energy level is above conduction band. The difference between Fermi level in c-Si and poly-Si induces a valence band offset and results in the reduction of the hole conductivity, thence, the selectivity for electrons is achieved [22]. Photo-generated holes close to the junction will be rejected from the interface and pushed back to the bulk, it reduces the recombination probability and increases the lifetime of minority carriers. When it comes to p-type poly-Si passivating contacts, the Fermi energy level in poly-Si is below valence band. The conduction band offset repels electrons from the c-Si/poly-Si interface to the bulk and causes a strong field-effect passivation for minority carriers.

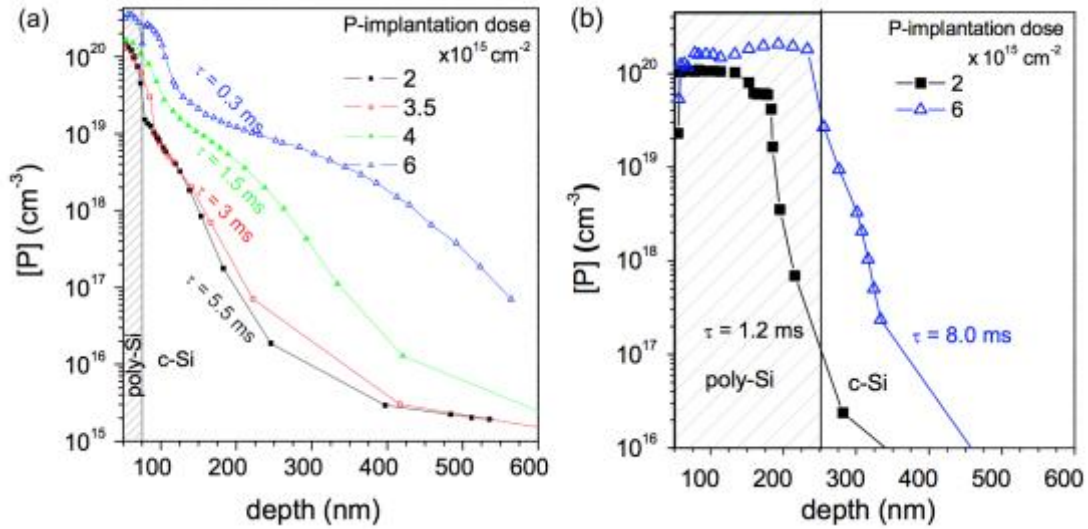


Figure 16 Phosphorous distributions at poly-Si/c-Si interface at different implantation dose (a) with 75 nm poly-Si and annealing in N₂ atmosphere at 850 °C for 90 min [10] and (b) with 250 nm poly-Si and annealing in O₂ atmosphere at 950 °C for 5 min [10].

According to the previous experiment results of Yang et al. [10], the relation between implantation dose and dopants distribution after annealing is given in Figure 16. When the implantation dose is too high, dopants will diffuse too deep into c-Si. Although selectively is achieved for both emitter and BSF, the indistinct dopants concentration step, as it is depicted in Figure 16 (a), leads to a weak band bending at c-Si/poly-Si interface. Meanwhile, the high dopant concentration in c-Si surface results in a high Auger recombination rate, as a consequence, leading to a poor passivation. However, when dopants are limited to the shallow area in poly-Si, there is less selectivity at poly-Si/c-Si interface (see Figure 16 (b)). The weak electric field does not reduce minority carrier concentration to an ideal value at c-Si/poly-Si interface. Minority carriers also have chances tunnel through the ultra-thin SiO₂ layer and diffuse to poly-Si layer, and then they will recombine due to the high concentration of majority carriers. Therefore, high recombination rate results in poor passivation. This explains the decrease in minority carrier lifetime and the increase of dark saturation current whenever dose is higher or lower than the optimal value. For example, phosphorous atoms diffuse deep into c-Si with dose at $1 \times 10^{16}/\text{cm}^2$, such as sample 9, the weak band bending at c-Si/poly-Si interface in combination with high Auger recombination rate results in low passivation quality. When phosphorous implantation dose is $2 \times 10^{15}/\text{cm}^2$, for sample 1, the weak electric field allows minority carrier holes reach c-Si/poly-Si interface and recombine there because of the high phosphorous concentration in poly-Si.

3.2 Effect of annealing on poly-Si passivation

The annealing time is crucial to the dopant profile which can be figured out from Figure 17 [10]. Its influence on the passivation properties is discussed in the last section, 3.1. It is shown that the dopant will diffuse deeply into c-Si when the annealing time increases with the same poly-Si thickness, implantation dose and energy.

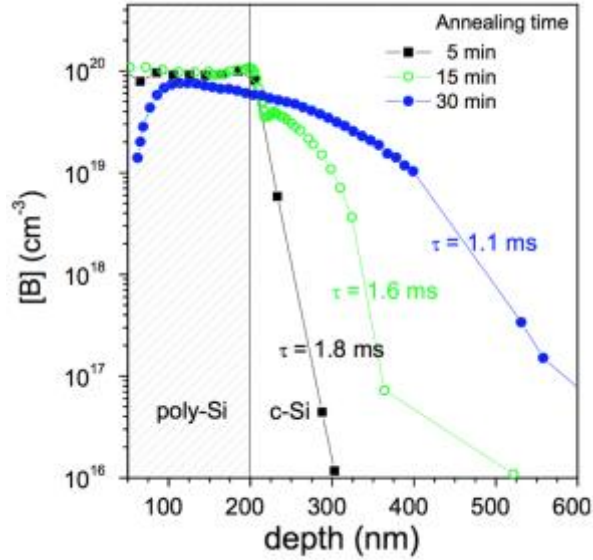


Figure 17 The dopant profiles for boron implanted into poly-Si, the implantation dose is $5 \times 10^{15}/\text{cm}^2$, energy is 5 keV and 950 °C annealing at O_2 atmosphere [10].

Samples for annealing condition test have the same structure as that for implantation dose test which is shown in Figure 11. The same tunnel SiO_2 formed by standard cleaning, and a-Si formed by LPCVD as previous test are used. The implantation dose and energy for phosphorous are $6 \times 10^{15}/\text{cm}^2$ and 20 keV, and they are $5 \times 10^{15}/\text{cm}^2$ and 5 keV for boron. The reason for choosing these values is that it is the standard recipe for previous solar cell run [10], therefore it is convenient for comparison with previous results. Meanwhile, higher ion-implantation dose in poly-Si decrease the resistivity for lateral current and increase FF in solar cells. The annealing can be divided into two steps in this test, the first one is 950 °C annealing for 5 minutes in O_2 atmosphere, the second one is 850 °C annealing for 90 minutes in N_2 atmosphere. The two steps annealing is implemented in solar cell fabrication process where the first annealing is to activate the dopants in LPCVD a-Si and poly-crystallize the LPCVD a-Si, in step 7 in the solar cell process, shown in Figure 13, section 2.4. After the first annealing, dopants are implanted on textured front surface for the formation of FSF. Then, the second annealing is performed to activate dopants in FSF, in step 7 in the solar cell process, shown in Figure 13, section 2.4. Compare to the first annealing step, the second annealing steps has lower temperature which is to limit the diffusion of phosphorous atoms to c-Si, since shallow profile with a low surface concentration can enhance J_{sc} according to the research by Xiao et al. [40].

Samples with n-type and p-type poly-Si are tested at three conditions: no annealing, only the first annealing and both the first and the second annealing. The test conditions and results of passivation properties are shown in Table 2.

Table 2 Passivation of poly-Si layers with different annealing condition.

Sample	Dopant	First annealing			Second annealing			Passivation		
		Temperature [°C]	Time [min]	O ₂ /N ₂	Temperature [°C]	Time [min]	O ₂ /N ₂	Lifetime [us]	J ₀ [fA/cm ²]	i-V _{oc} [mV]
14	P		~*			~		Not measurable		
15	P	950	5	O ₂		~		13648	5.7	>730
16	P	950	5	O ₂	850	90	N ₂	5575	6.25	>730
17	B		~			~		Not measurable		
18	B	950	5	O ₂		~		4594	14.15	711
19	B	950	5	O ₂	850	90	N ₂	1875	11.8	707

*~ no annealing is performed.

For both p-type and n-type poly-Si, the lifetime cannot even be measured when there is no annealing after implantation (sample 14 and 17). We suggest the explanation is that no chemical bonds are formed between dopants and native atoms after implantation and most dopants are in the very shallow surface of poly-Si, around 30 nm if no annealing is performed [41]. As dopants are not activated, we propose the energy level in semiconductor stay the same and therefore there is no selectivity for one certain carrier. Therefore, no field-effect passivation is established at c-Si/poly-Si interface since the shallow dopant profile and non-activated chemical bonds.

Then, for samples only experienced the first annealing (sample 15 and 18), the lifetime for n-type sample reach 13.6 ms and V_{oc} is higher than 730 mV. In other words, it has excellent passivation. For p-type poly-Si, the significant improvement on passivation can also be observed. After annealing at 950 °C for 5 minutes, dopants in the shallow surface of poly-Si are driven into the deep of poly-Si and a small part into c-Si, which cause a strong band bending in c-Si/poly-Si interface as is shown in Figure 17. Then, a strong field effect passivation is formed at interface repelling minority carriers from recombination at interface. It is reported by some researchers that 900 °C annealing results in poor surface passivation with p-type poly-Si [39][42], and 950 °C annealing will induce disruption of tunnel SiO₂ [27]. The influence of tunnel SiO₂ on the passivation will be discussed in next section.

The difference in passivation for n-type and p-type poly-Si may attribute to the light boron atoms are easier to diffuse through the tunnel oxide layer [38], and few boron atoms are isolated in grain boundaries [43] and create more defects in SiO₂ layer [44]. One thing that needs to be pointed out is the difference between the results in Table 2 and Table 1. For example, sample 5 in Table 1 and sample 14 in Table 2 experience the same process but the passivation is of significant difference, this is also the case for sample 13 in Table 1 and sample 18 in Table 2. Samples in Table 2 have obvious better passivation than that in Table 1 where the difference lays on the NAOS process. Although all the tunnel oxide is formed by standard cleaning process in Else Kooi laboratory, the standard cleaning line in C100, this nitric acid is not the same whenever the standard cleaning is performed. After the usage of standard cleaning bath for several times, the solution is not the same as before. Therefore, the physical properties of tunnel SiO₂ changes which lead to the variation of chemical passivation, which is the main motivation of the next session, developing a stable approach for tunnel SiO₂ formation.

For sample 16 and 19, which experience both the first annealing and the second annealing steps,

present decrease in passivation performance compared to sample 15 and 18. The lifetime is less than the half of that of 15 and 18. This is because dopants diffuse too deep into c-Si and lower the minority carrier lifetime. Although the lifetime decrease a lot, J_0 and $i-V_{OC}$ reduce slightly. The change in passivation is still acceptable as two-steps annealing is imperative for the solar cell fabrication. Compare to sample 18, sample 19 has lower J_0 but also a low $i-V_{OC}$. This is due to the implied V_{OC} is calculated from the minority carrier density and largely depends on the sheet resistivity of sample. And it does not have a physical meaning for samples without pn junction, such as symmetrical sample with structure shown in Figure 12. Meanwhile, phosphorous has low segregation coefficient then the wafer resistivity is not uniform on the whole silicon ingot [45], which means that the $i-V_{OC}$ is not the same for wafer on different region of the ingot even though they go through the same process. J_0 is calculated from the decay of the minority carrier concentration and it is more reliable that reflect the passivation quality.

3.3 Optimization of tunnel SiO₂

There are several ways of forming tunnel oxide, such as wet-chemical oxide, UV/O₃ oxide and thermal oxide [40]. The wet-chemical oxidation in HNO₃ is a self-limiting process which means that oxide thickness keeps the same after saturated [46][47]. In this work, only standard wet-chemical oxide formed by HNO₃ is studied. As it is explained in the previous section, the tunnel oxide formed by standard cleaning, see the next paragraph for the detailed steps, is not stable. The objective of the tunnel oxide test is to find a stable wet-chemical oxidation which provides excellent passivation.

For sample preparation, the structure is shown in Figure 11 and the only variable is the way of SiO₂ formation. Three different NAOS processes are:

1. Standard cleaning:
 - (1) 10 minutes in 99%, room temperature HNO₃ + 5 minutes rinsing in DI water,
 - (2) 10 minutes in 67.5%, 110 °C HNO₃ + 5 minutes rinsing in DI water.
2. 67.5%, room temperature HNO₃ with variable immersion time + 5 minutes rinsing in DI water.

Other steps are kept the same: the LPCVD a-Si thickness is 250nm, the ion-implantation dose is $6 \times 10^{15}/\text{cm}^2$ and energy is 20 keV for phosphorous, and $5 \times 10^{15}/\text{cm}^2$ and 5 keV for boron. Only one annealing step is implemented which is the five-minute annealing at 950 °C in O₂ atmosphere. It means that all the other process steps except for the tunnel oxide formation are the same as sample 15 and 18 in Table 2 for n-type poly-Si samples and n-type poly-Si samples, separately. The passivation performance is shown in Table 3.

Table 3 Passivation of poly-Si passivation structure with different tunnel SiO₂ formation.

Sample	Dopant	SiO ₂		Passivation		
		HNO ₃	Time [min]	Lifetime [us]	J ₀ [fA/cm ²]	i-V _{OC} [mV]
20	P	Standard cleaning		5212	5.7	725
21	P	Standard cleaning		2909	17.5	707
22	B	Standard cleaning		5346	12	716
23	B	Standard cleaning		361	15.7	668
24	P	67.5%	5	593	40.8	688
25	P	67.5%	10	917	28	698
26	P	67.5%	15	1791	15.7	711
27	P	67.5%	30	3362	8.5	717
28	P	67.5%	45	12780	7.9	>730
29	P	67.5%	60	18164	4.5	>730
30	P	67.5%	90	16021	5.65	>730
31	P	67.5%	120	5260	5.1	726
32	B	67.5%	5	136	73.5	640
33	B	67.5%	10	114	71.5	637
34	B	67.5%	15	189	70	651
35	B	67.5%	30	420	5.5	672
36	B	67.5%	45	3087	22.6	703
37	B	67.5%	60	5503	12.9	714
38	B	67.5%	90	4082	17.2	709
39	B	67.5%	120	4361	14.7	711

From the results for sample 20-23 which were prepared in different days via standard cleaning, it is apparent that passivation performance fluctuates while the SiO₂ is formed via standard cleaning. The best J₀ are 5.7 fA/cm² for n-type and 12 fA/cm² for p-type, while i-V_{OC} arrives 725 mV and 716 mV for n-type and p-type, separately. However, the passivation can also be poor sometimes as the usage history of nitric acid of standard cleaning is unknown every time NAOS is performed.

To solve this problem, 67.5% HNO₃ is used separately to test the tunnel oxide quality. And 67.5% HNO₃ is fresh solution and prepared in separate quartz containers only for the formation of tunnel SiO₂ on c-Si, which promises the experimental repeatability. Sample 24 to 39 are immersed in 67.5% HNO₃ with time varying from 5 minutes to 120 minutes. The best passivation occurs when immersion time is 60 minutes both for n-type and p-type samples, which are sample 29 and 37. The dark saturation current density is only 4.5 fA/cm with lifetime reach 18 ms, and i-V_{OC} is higher than 730 mV for n-type (sample 29) which are highlighted in Table 3. The passivation quality is even better than the best that carried out by standard cleaning (sample 15 in Table 2). For p-type, passivation of sample 37 is at the same level that of sample 22.

Since the SiO₂ formation in HNO₃ solution is a self-limiting process [46], the increase of immersion time will not change the thickness of tunnel oxide but the density may increase, and the stoichiometry may change. In our case, the thickness of tunnel SiO₂ is 1.5 nm and remains intact after annealing at 950 °C for 5 minutes according to the measurement via TEM by Yang [10] (see Figure 18). Although this SiO₂

is formed by standard cleaning in EKL, it proves the thermal stability of the NAOS SiO_2 .

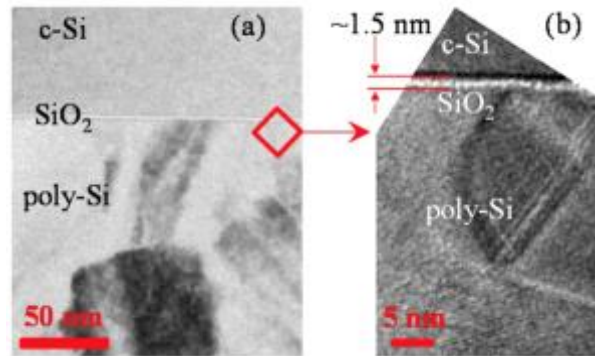


Figure 18 TEM picture of the c-Si/poly-Si interface in scale of (a) 50-nm scale and (b) 5-nm scale [10].

Therefore, the variation of passivation with immersion may attribute to the change in the density of tunnel SiO_2 , as well as the stoichiometry. When the immersion time is short, the SiO_2 is not dense enough and it is easy to be disrupted during high-temperature annealing, especially for temperature higher than 900°C . The pin-holes in SiO_2 layer induces the direct contact of doped poly-Si layer and c-Si substrate, chemical passivation is lost and recombination rate increase dramatically [42][48]. Those pin-holes on oxide are not always bad for passivation, current flow through pin-holes may even dominant when the thickness of SiO_2 is higher than 2 nm when tunneling is not easy to happen [29]. With the increase of immersion time, the SiO_2 density increases and it is not easy to be disrupted, thence, chemical passivation remains after annealing. Although some researchers report that wet-chemical oxide combined with high temperature ($>900^\circ\text{C}$) annealing will result in poor passivation [27][39][42]. Passivation for sample 29 and 37 can be assumed that the dense wet-chemical oxide is thermally stable therefore it remains intact after 950°C annealing. As thick (>2 nm) thermal oxide layer is also used in poly-Si passivating contacts and it also provides excellent passivation after 1050°C annealing [29][33][40]. Another benefit of increasing tunnel oxide density is that it may minimize the diffusion depth of dopants from poly-Si into c-Si during the high temperature annealing, this reduces the Auger recombination in the c-Si at poly-Si/c-Si interface. The increase of immersion of immersion time may change the stoichiometry of silicon oxide which leads to a better lattice match of SiO_x and c-Si. With the continuous increase of immersion time, tunnel SiO_2 may become too dense and even reduce the probability for majority carrier to tunnel through, such as sample 31 and 39. The dopants profiles at c-Si/poly-Si interface can be measured, thus the band bending at interface can be derived to verify the carrier behavior at interface. Meanwhile, the x-ray photoelectron spectroscopy (XPS) can be used to measure the thickness, density, and stoichiometry of the tunnel oxide formed via different immersion time in nitric acid.

The junction resistance of poly-Si/c-Si is measured in case a too dense or maybe thicker SiO_2 may increase contact resistance and thence, lowering the FF in solar cell. The reason is that the SiO_2 is a dielectric material which blocks the current flow with the thickness higher than certain value. It gives rise to the contact resistance of c-Si/poly-Si which one of the sources of the series resistance. Finally, FF will decrease with the increase of R_s . The contact resistance is measured by TLM method both for Al/n-type poly-Si/c-Si and Al/p-type poly-Si/c-Si and the results are shown in Figure 19. The current flow in test samples during TLM measurement are Al/ doped poly-Si/ SiO_2 / c-Si/ SiO_2 / doped poly-Si/ Al which is to simulate the real current flow in solar cells with the current path of c-Si/ SiO_2 / doped poly-Si/ Al.

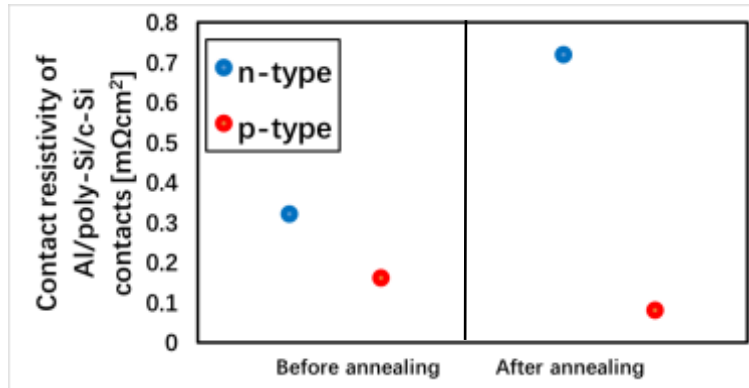


Figure 19 Specific contact resistance of Al/ doped poly-Si/ c-Si contacts before post annealing and after post annealing at 600 °C for 30s.

The 600 °C annealing is used to enhance the passivation of FSF/BSF and emitter due to the hydrogenation of the c-Si interfaces provided by the hydrogen within the passivation layers. The contact resistivity for Al/n-type poly-Si/c-Si contact is about 0.3 mΩ/cm² before annealing and it increases to 0.7 mΩ/cm² after annealing at 600 °C for 30 s. This increase is attributed to the formation of Al spikes at the Al-Si interface at high temperature. At the same time, the produce aluminum-silicon alloy, which starts to form at 577 °C [40], can help the formation of ohmic contact to reduce the contact resistance, which is reflected in the result of p-type poly-Si samples. Therefore, a carefully control of the annealing temperature and time, the balance between Al spikes and Al/Si alloy, deserve a study in order to obtain the optimal contact resistance for contacting both n-type and p-type poly-Si.

For Al/n-type poly-Si/c-Si contact, the contact resistivity is almost the same before and after annealing, with a value around 0.3 mΩ/cm². The measurement results are in agreement with the experiment result of Michael et al. [33] which are around 0.6 mΩ/cm² for Al/ n-type poly-Si/ c-Si contact and 0.2 mΩ/cm² for Al/ p-type poly-Si/ c-Si contact. This means that tunnel SiO₂ formed by 60-minute oxidation in HNO₃ does not cause an increase in contact resistance, therefore, also the solar cell series resistance.

3.4 Solar cells

The fabrication process for IBC solar cells with poly-Si passivating contacts is discussed in section 2.4. Here, only some details are introduced. The tunnel oxide is formed via standard cleaning, and thermal oxide is used as passivation layer on FSF. For FSF, the implantation parameters are 1×10^{14} /cm² and 10 keV. The implantation dose and energy for BSF are 6×10^{15} /cm² and 20 keV, for emitter are 5×10^{15} /cm² and 5 keV. Although the results in section 3.1 show that implantation dose at 4×10^{15} /cm² offers the best passivation properties, the old recipe mentioned above, that was used by Yang [10] (see Figure 20 (a)) is still implemented in this solar cell run. This is for the convenience of comparison with previous results and for variable control. The only difference for some solar cells is the thin Al₂O₃ layer deposited by ALD on poly-Si at back side which is shown in Figure 20 (b). Although Al₂O₃ has negative charge and it is not a good candidate for passivating n-type wafer, it provides enough hydrogen atoms during deposition and provides hydrogenation to poly-Si as well as poly-Si/SiO₂/c-Si interface. Table 4 reports the results of IBC solar cells.

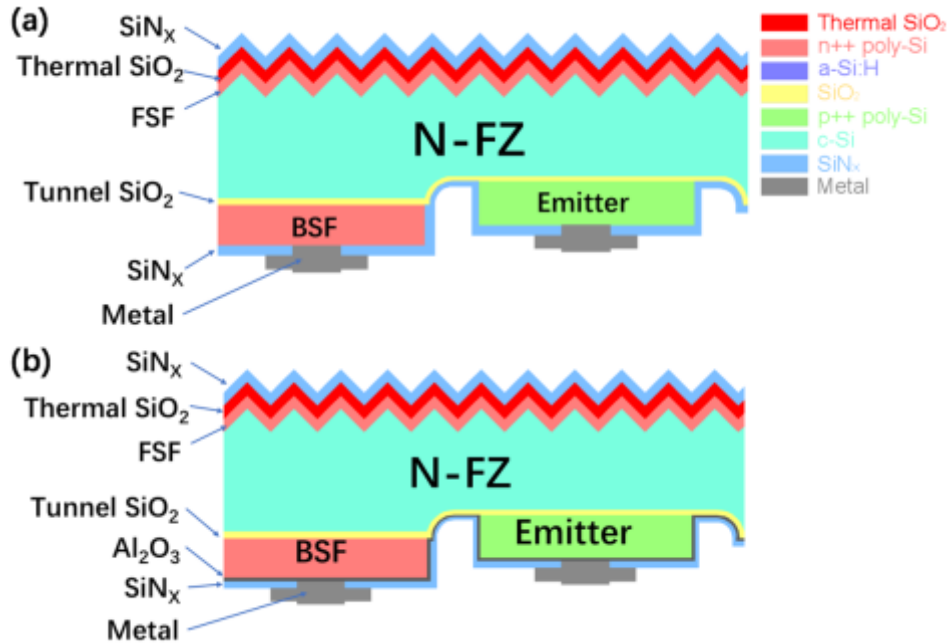


Figure 20 Schematic IBC solar cell with poly-Si passivating contacts (a). no Al_2O_3 at back side (b) Al_2O_3 at back side.

Table 4 Performance of poly-Si passivating contacts IBC solar cells.

Cell number	Area [cm^2]	Al_2O_3	V_{oc} [mV]	J_{sc} [mA/cm^2]	FF [%]	η [%]
1	9	Yes	670	38.4	78	20.01
2	0.72	Yes	665	37.1	81	20
3	9	No	665	36	77.9	18.69
4	0.72	No	670	37.1	83.2	20.7
5	9	No	692	39.2	78.3	21.2

In Table 4, cell 1 to 4 are cells that fabricated in the same solar cell run, where cell 1 and 2 has the structure shown in Figure 20 (b), a thin layer of Al_2O_3 between poly-Si and SiN_x at back side was inserted. Cell 3 and 4 have structure which is shown in Figure 20 (a). The results of cell number 5, which have already been published [10], are shown in the table as a reference as it has the same structure as cell number 3 and 4. Compare the performance between cell 1 and cell 2, cell 2 has obvious higher FF than cell 1. The difference in FF is due to the metallization on the back side, cell 2 has a smaller area than cell 1 and thus it benefits from a lower series resistance of metal fingers. This also happens to cell 3 and 4. The rise in FF due to the decrease in solar cell area indicates that the metallization steps limit the large area solar cell performance in the means of series resistance of the metal fingers, which can be further improved by a delicate design of metal fingers distribution and its thickness. However, a loss in J_{sc} is observed. Since cell 1 and 2 are based on the same wafer, thus all the structures are the same. Therefore, the loss in J_{sc} may attribute to the non-uniformity of the SiN_x during deposition. The thickness of SiN_x layer used in the cell as antireflection coating is calculated according to the destructive interference and AM1.5 spectrum, a non-optimal thickness will reduce the light trapping in solar cell

and hence a low J_{SC} is obtained.

For V_{OC} , there is almost no difference between cell 1, 2 and cell 3, 4, which are all around 670 mV. This means that although Al_2O_3 in cell 3 and 4 give hydrogenation to poly-Si and c-Si which reduces the recombination rate at the surface, the negative corona charges in Al_2O_3 reduce the electron collect efficiency. The benefit is compensated by the drawback of Al_2O_3 and eventually, results in no effect on V_{OC} . When compare all cells from 1 to 4 with cell 5, cell 5 has much higher V_{OC} and J_{SC} . Since the process steps and recipes are the same for cell 1, 2 and 5, the variation can only be the uncertainty during the process. For example, the unstable passivation given by standard cleaning tunnel SiO_2 has a huge impact on the passivation properties of poly-Si, and therefore on the solar cell performance. Thus, to reduce the uncertainty, NAOS based SiO_2 by 60 minutes 67.5% HNO_3 will be implemented in next solar cell run. Meanwhile, to rise the FF, metallization can be improved to reduce series resistance.

4

Optimization of Front Surface Passivation

For IBC solar cells with poly-Si passivating contacts, the solar cell performance is not only affected by poly-Si passivating contacts at rear side, passivation on front surface is also essential for raising efficiency. The front surface consists of the ion-implanted front surface field, a passivation layer and a 75 nm thick SiN_x layer as anti-reflection coating. In this chapter, the optimization of the FSF passivation focus mainly on optimizing the passivation layer, PECVD a-Si:H, the influence of implantation dose of FSF on the passivating properties. And finally, their effects on the solar cell performance are also discussed.

4.1 Optimization of FSF passivation

In the last chapter, the highest V_{OC} for the solar cell is only 670 mV. The low V_{OC} mainly due to the unstable passivation performance of tunnel oxide and the non-optimal passivation on front surface. The objective of this section is to improve the performance of front surface field passivation. To optimize the passivation on FSF, a-Si:H is chosen to replace the previously used thermal oxide before. Hydrogenated amorphous silicon has already been proved as an excellent material which provides good surface passivation and enables V_{OC} of 750 mV [23]. In this work, the optimization of a-Si:H on FSF lays on its deposition temperature and thickness. There are two facts that need to be taken into consideration: the electrical and optical effect of the a-Si:H on the solar cell performance, and the influence of FSF implantation dose on its passivation properties and the lateral carrier transport in the solar cell. To be more in detail, a too thick passivation layer on front side may induce a high parasitic absorption and hence lower J_{SC} . But a too thin passivation layer may not have enough passivation then a low V_{OC} will be obtained. Since most light at short wavelength has higher absorption coefficient, it can be absorbed and generate e-h pairs close to the surface. The phosphorous implanted FSF is to enhance the blue response of the solar cell and increase J_{SC} . Holes generated near the surface will be rejected by electric field to the bulk therefore recombination rate is reduced. However, a strong electric field required a high dopant concentration in c-Si near surface, a too high doping will increase Auger recombination. An optimal implantation dose to FSF improves the both V_{OC} and J_{SC} , therefore, different implantation doses are tested by symmetrical tests. The symmetric test is carried out with the structure shown in Figure 12, the passivation layer is a-Si:H and different deposition temperature and thickness in combination with different FSF implantation dose are tested to obtain an optimal passivation performance. The results are reported in Figure 21.

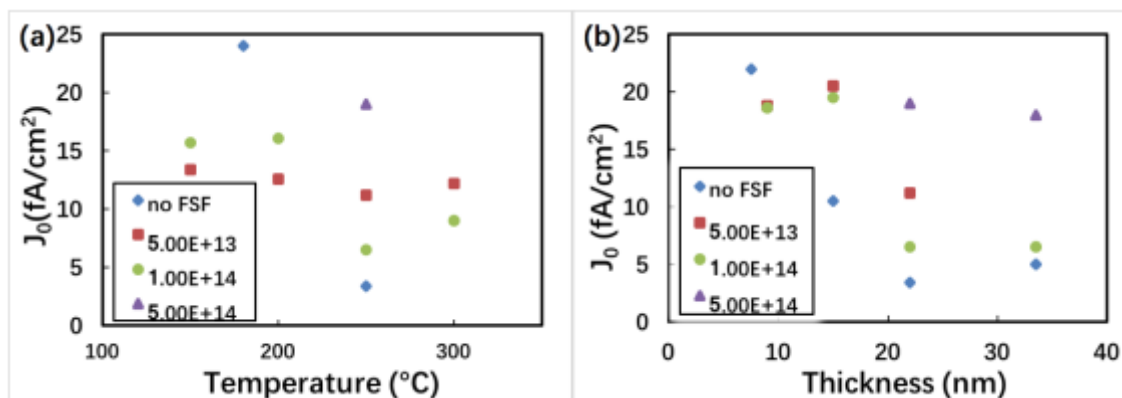


Figure 21 Surface passivation quality of phosphorous implanted textured n-FZ Si wafer as a function of the a-Si:H (a) deposition temperature with fixed deposition time of 36s and (b) deposition thickness with fixed deposition temperature of 250 $^{\circ}\text{C}$.

The temperature series symmetric test is to find out an optimal deposition temperature of a-Si:H with different FSF implantation dose (see Figure 21 (a)). The lowest J_0 among all samples occurs when a-Si:H is deposited on a no ion-implanted textured n-FZ wafer at 250 $^{\circ}\text{C}$ for 36s, with only 3.4 fA/cm^2 . The reason why no implantation samples have lower J_0 is that dopants implanted in c-Si will cause defects and increase recombination rate, however, this is the case for samples with P-implantation. For samples with P-implantation, the lowest J_0 is 6.5 fA/cm^2 for sample $1 \times 10^{14}/\text{cm}^2$ implantation dose, on which the a-Si:H is also deposited at 250 $^{\circ}\text{C}$ for 36s. For samples with $5 \times 10^{13}/\text{cm}^2$ implantation dose, J_0 does not show obvious fluctuation to deposition temperature, but the lowest value still happens with 250 $^{\circ}\text{C}$ deposition which is 11.2 fA/cm^2 . Therefore, the optimal a-Si:H deposition temperature for textured front surface passivation is around 250 $^{\circ}\text{C}$ which is consistent with the experiment results of Dauwe et al [9]. When a-Si:H is deposited at low temperature, lower than 200 $^{\circ}\text{C}$, the mobility of hydrogen is low thence the dangling bonds at interface are not completely passivated. With the increase of deposition temperature, the surface passivation performance improved as the diffusion of hydrogen atoms to the interface. A high deposition temperature (300 $^{\circ}\text{C}$) decreases the J_0 compare to that of 250 $^{\circ}\text{C}$. This may be attribute to the accumulation of the hydrogen in defects as the high mobility at high temperature [40].

After determining the optimal deposition temperature of the PECVD a-Si:H layer, its thickness of a-Si:H needs to be optimized. Different thicknesses of a-Si:H layers are deposited on textured wafers with different FSF implantation doses, the results are shown in Figure 21 (b). However, the lowest J_0 for samples with and without P-implantation are still the same as in Figure 21 (a). With 22nm a-Si:H, the best J_0 is 3.4 fA/cm^2 for no FSF sample and 6.5 fA/cm^2 for P-implantation sample with the dose at $1 \times 10^{14}/\text{cm}^2$. When further increase the a-Si:H thickness to 34 nm, J_0 does not decrease but the parasitic absorption will be increased in solar cells, therefore, thicker a-Si:H on front side is not a good optional for solar cells. When a-Si:H becomes thinner, J_0 for sample with $1 \times 10^{14}/\text{cm}^2$ P-implantation dose increase to around 20 fA/cm^2 for both 15 nm and 9 nm thickness, which is the same for implantation dose at $5 \times 10^{13}/\text{cm}^2$. Although thinner a-Si:H layer on FSF is not the optimum for front surface passivation, it is still worthy to be implemented in solar cells for lower parasitic absorption and eventually a higher J_{sc} .

4.2 Solar cells

In this solar cell run, the passivation layer on both FSF and back side are different compared to the solar cell in section 3.4. Moreover, the NAOS SiO_2 is also different in order to obtain a tunnel oxide layer with more stable chemical passivation. The basic process flow is the same as the solar cell in section 3.4, the implantation dose for BSF, emitter and FSF are $6 \times 10^{15}/\text{cm}^2$, $5 \times 10^{15}/\text{cm}^2$ and $1 \times 10^{14}/\text{cm}^2$, separately. The differences are that the front side is passivated by 22nm a-Si:H deposited at 250 °C. At back side of the cell, on poly-Si layers the growth of an additional 6.5 nm thick a-Si:H is for supplying hydrogen atoms to poly-Si and c-Si for extra enhancement of their passivation. The tunnel oxide is formed by 1-hour immersion in 67.5% HNO_3 for stable passivation performance. The structure of such a solar cell is shown in Figure 22. With these optimized condition, solar cell efficiency of 22.1% is achieved. The performance of solar cells is reported in Table 5.

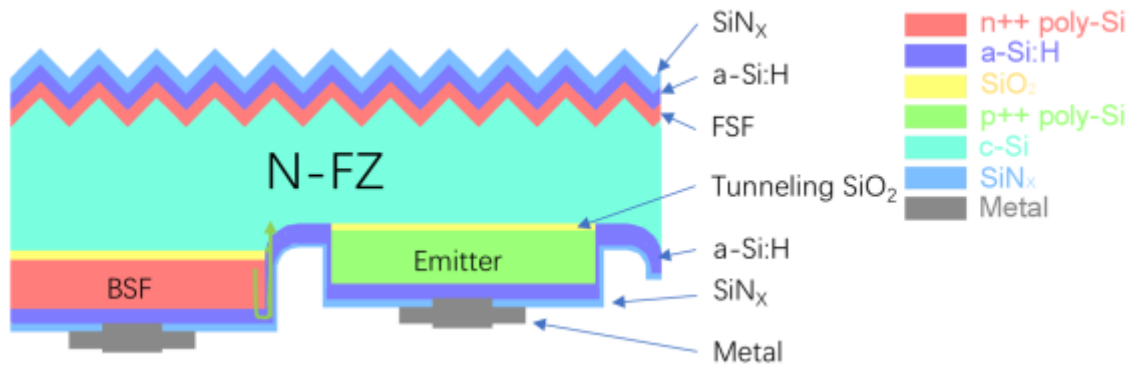


Figure 22 Schematic of poly-Si passivating contacts IBC solar cell with optimized front and back passivation layer and tunnel oxide is formed in 67.5% HNO_3 for 1 hour.

Table 5 Performance of poly-Si passivating contacts IBC solar cells with optimized front and back passivation and different FSF implantation dose.

Cell number	Area [cm^2]	FSF implantation dose [$/\text{cm}^2$]	V_{oc} [mV]	J_{sc} [mA/cm^2]	FF [%]	η [%]
1	9	No FSF	683	37.3	72.3	18.4
2	9	$1e14$	705	38.5	69.7	18.9
3	0.72	$1e14$	709	40.7	76.4	22.1
4	9	$5e14$	694	38	66.7	17.6

Table 5 shows the characteristics of solar cells with different FSF implantation dose and cell area. When FSF implantation dose is $1 \times 10^{14}/\text{cm}^2$, a high V_{oc} value is obtained which is 705 mV for a 9 cm^2 cell and 709 mV for a 0.72 cm^2 cell. The high V_{oc} can be owed to the low J_0 at FSF after employing a-Si:H as passivation layer, as it the J_0 value is $6.5 \text{ fA}/\text{cm}^2$ (see Figure 21). For cell 3, the J_{sc} is $40.7 \text{ mA}/\text{cm}^2$ and it is much higher compared to cell 1 and 4, which has no FSF and $5 \times 10^{14}/\text{cm}^2$ FSF implantation dose, separately. With an optimal phosphorous-implanted FSF, the minority carrier, holes, recombination rate at front surface is reduced since they are repelled by electric field. Meanwhile, the FSF enhance the stability of passivation performance for short wavelength light as most of UV light will be absorbed near the surface. When there is no FSF, photo-generated carriers cannot be pushed to bulk and

recombine, especially for poor blue response. For these reason, J_{sc} for cell 1 is only 37.3 mA/cm^2 and the low passivation at front surface leads to a low V_{oc} which is 683 mV . The EQE of cell 3 is shown in Figure 23 (a), 1-R curve and 1-R-T curve are also plotted. The reflection loss at long wavelength is still high, as 1-R curve keeps decreasing after 600 nm . This means the SiN_x layer thickness on the top of the surface still needs to be optimized, or double anti-reflection coatings can be employed to reduce reflection at long wavelength. The 1-R and 1-R-T curves are overlapped in the wavelength range from 300 to 1100 nm , and it shows that there is almost transmittance for the light that the c-Si can absorb. The difference between EQE and 1-R-T curves occurs at both short wavelength ($<500 \text{ nm}$) and long wavelength ($>1000 \text{ nm}$). At short wavelength, the difference is due to the parasitic absorption in a-Si:H and SiN_x layer on FSF. The a-Si:H is a direct bandgap material and it has high absorption coefficient compared to c-Si, hence a very thin layer of a-Si:H can cause a high optical loss at short wavelength. This gives indication to the improvements on next solar cell run, thinner a-Si:H layer on FSF should be implemented to increase J_{sc} . In the range of long wavelength, the parasitic absorption arises owing to the 250-nm thickness highly-doped poly-Si. The absorption coefficient increased due to the existence of high-concentration dopants. Thinner poly-Si can be deposited, however, the change of poly-Si thickness is accompanied by the adaption of implantation dose and annealing condition. Moreover, materials with lower absorption coefficient can also be tried.

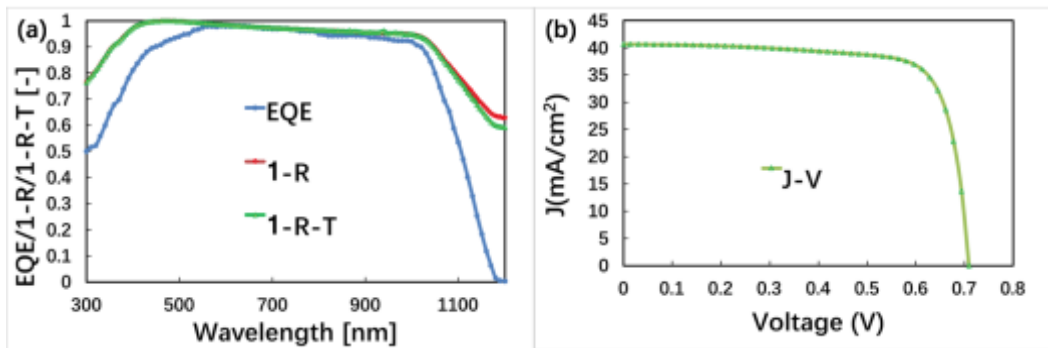


Figure 23 (a) EQE, 1-R, 1-R-T of cell 3 (b) J-V curve of cell 3.

When the FSF implantation dose increase to $5 \times 10^{14} / \text{cm}^2$, V_{oc} reduces to 694 mV which is 11 mV lower compared to cell 2. The reduction in V_{oc} is attributed to high Auger recombination at FSF, with J_0 at FSF equals to 19 fA/cm^2 according to the measurement results in Figure 21, which is induced by high dopant concentration. The high FSF implantation dose will also cause a deep phosphorous diffusion depth after annealing, which reduces the blue response and lower the J_{sc} to 38 mA/cm^2 . The FF for 9 cm^2 cells are all lower than 73% , and it increases to 76.4% when the cell area decreases to 0.72 cm^2 . The effect of small cell has been explained in section 3.4. Figure 23 (b) shows the J-V curve of cell 3, the curve is not flat at low bias voltage indicates that the cell suffers from shunting problem. The pFF of cell 3 is measured from $\text{suns-}V_{oc}$ is 79.6% , which also offer an evidence of shunting. The shunting problem in solar cells may be attributed to the current flow through a-Si:H. The green arrow in Figure 22 depicts the possible carrier path, charge carriers in emitter and BSF may flow through a-Si:H and back to c-Si and induces current shunt. This can be avoided by depositing an insulating layer under a-Si:H on trenches between BSF and emitter which will be discussed in next section.

4.3 Solving the shunt in solar cells

The shunt caused by a-Si:H layer on back side induces a reduction on FF and it is improved by keeping

the underneath thermal oxide layer obtained during the annealing step (see Figure 24 (a)). The thermal oxide is formed during the second annealing step, which is 850 °C for 90 minutes, and it is also formed on BSF and emitter. The designed thermal oxide is only in the trenches between BSF and emitter, this requires a patterning step to define the remaining thermal oxide area by photolithography. However, the mask used in this lithography step can only open the thermal oxide under metal contacts. Therefore, the real solar cells have the structure shown in Figure 24 (b). The efficiency of solar cells reaches 21.94% for a 9 cm² cell and 22.5% for a 0.72 cm² cell with improved shunt path isolation. The results are presented in Table 6, where cell 1 to cell 3 have the structure shown in Figure 24 (b). The BSF and emitter occupy 38% and 62% of the total back area, separately. The different proportion of emitter and BSF is due to the relatively low conductivity of the holes in p⁺⁺ region compared to electrons in n⁺⁺ region, higher emitter occupation is convenient for hole collection. Cell 4 has reversed emitter and BSF area, to be more specific, BSF in Figure 24 (b) is emitter for cell 4 and emitter in Figure 24 is BSF. The exchange of BSF and emitter ratio is motivated by the fact that n-type poly-Si passivating contacts offer better passivation compared to that of p-type poly-Si.

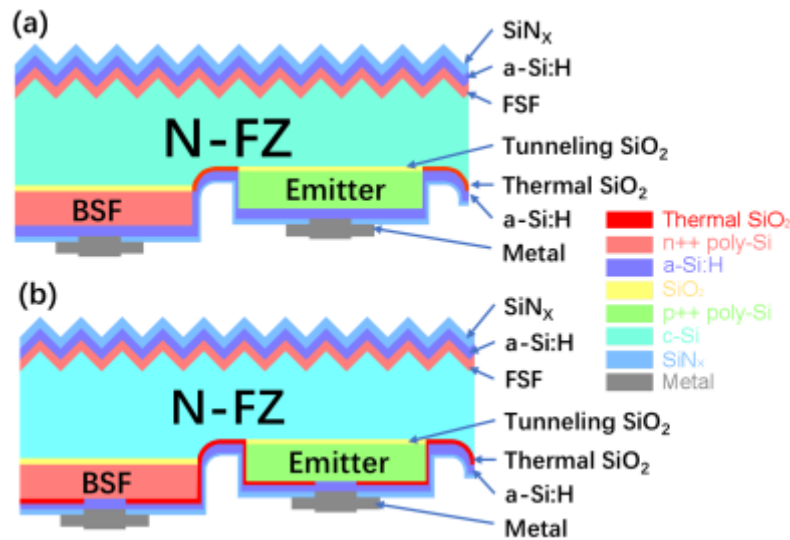


Figure 24 Schematic of poly-Si passivating contacts IBC solar cell with (a) ideal thermal oxide isolation (b) real thermal oxide isolation.

Table 6 Performance poly-Si passivating contacts IBC solar cell with real oxide isolation.

Cell number	Area [cm ²]	Emitter ratio [%]	V _{OC} [mV]	J _{SC} [mA/cm ²]	FF [%]	η [%]
1	9	62	696	39.6	79.6	21.94
2	0.72	62	681	41.3	80	22.5
3	0.72	62	676	37.3	81.7	20.62
4	9	38	685	39	79.3	21.25

It can be seen from the table that all cells have higher FF compared with cells in Table 5 after adding a thermal oxide layer for shunt prevention. The highest FF in this run is 81.7% for cell 3 with area of 0.72 cm², but it is still lower than the best FF (83.2%) in section 3.4. The difference in FF may lay on the a-Si:H layer at rear side while there is no a-Si:H in Figure 20(a). This thin layer gives a rise to series

resistance in solar cell and hence reduces FF. The V_{OC} of these four cells are apparently lower than cell 2 and 3 in Table 5, this can be attributed to the non-optimal distribution of thermal oxide at back side induced by the HF dip before the front side a-Si:H layer deposition. The thermal oxide on BSF and emitter does not offer a better chemical passivation compare to the a-Si:H. With $V_{OC}=696$ mV, $J_{SC}=39.6$ mA/cm² and FF=79.6, the 9 cm² cell 1 efficiency reach 21.94%. For cell 2, a high $J_{SC}=41.3$ mA/cm² is measured from J-V measurement, the rise in current compare to cell 1 may because of the non-uniformity deposition of SiN_x and a-Si:H layer on front surface which result in high optical performance. The rise in J_{SC} is not completely clear and it indicates that further experiment needs to be done to reduce optical loss at front side and its uniformity. For cell 4, the reversal of emitter and BSF does not offer a better passivation at back side but results in a 10mV loss of V_{OC} and a decrease of J_{SC} . The reduction in efficiency suggests that higher BSF coverage at back side does not give a better passivation for solar cell, at least for the coverage ratio of BSF to emitter at 0.62:0.38. This may because that low p-type emitter coverage is not good for current collection since the lower conductivity for holes in emitter compared to electrons in BSF.

Since the total J_0 consists of dark saturation current at BSF, emitter FSF and bulk, substitutes J_0 with J_0 from these four parts in equation 1.3:

$$V_{OC} = \frac{nkT}{q} \ln \left(\frac{J_{ph}}{J_0} + 1 \right) = \frac{nkT}{q} \ln \left(\frac{J_{ph}}{A^{BSF} J_0^{BSF} + A^{emitter} J_0^{emitter} + J_0^{FSF} + J_0^{Bulk}} + 1 \right) \quad (4.1)$$

where J_0^{BSF} , $J_0^{emitter}$, J_0^{FSF} and J_0^{Bulk} are dark saturation current associated to BSF, emitter, FSF and bulk, separately. A^{BSF} and $A^{emitter}$ are the area coverage of BSF and emitter. From the symmetrical test results, $J_0^{BSF} = 4.5$ fA/cm², $J_0^{emitter} = 11.8$ fA/cm², $J_0^{FSF} = 6.5$ fA/cm² and J_0^{Bulk} is around 10 fA/cm². Use $J_{ph} = 41.3$ mA/cm², V_{OC} can be as high as 725 mV with structure in Figure 24 (a). Therefore, the solar cell has potential to reach 24% efficiency.

4.4 Reduce the a-Si:H parasitic absorption

From the spectrum response of cell 3 in Table 5 that is shown in Figure 20, the huge difference between EQE and 1-R-T in short wavelength (<500 nm) indicates that the parasitic absorption in solar cell at front side cause a big J_{SC} loss. To obtain a high J_{SC} and rise the solar cell efficiency, thinner a-Si:H is employed on front side of the solar cell for a low parasitic absorption at short wavelength. Meanwhile, thicker a-Si is deposited on rear side attempting to enhance chemical passivation. The cell structure is still the same as that in section 4.3, which is depicted in Figure 24 (b). However, there was a problem happened during solar cell fabrication. In Figure 13, from step 2 to step 3, the exposed SiN_x barrier layer was not completely etched away. This remained SiN_x layer, in the thickness between a few nanometers to around ten nanometers, acts as a masking layer during the removal of the LPCVD a-Si layer in the emitter area. And as a result, a rough surface is formed on the c-Si surface in the area for emitter deposition which will dramatically decrease the emitter passivation. The results of cells with different a-Si thickness at FSF are shown in Table 7 and the corresponding EQE curves of these three cells are presented in Figure 25.

Table 7 Performance of solar cells respect to the variation of the thickness of a-Si:H passivation layer on FSF.

Cell number	Area [cm ²]	Thickness [nm]	V_{OC} [mV]	J_{SC} [mA/cm ²]	FF [%]	η [%]
1	9	22	679	37.1	76.5	19.2

2	9	15	676	36.1	76	18.5
3	9	9	675	36.8	75	18.6

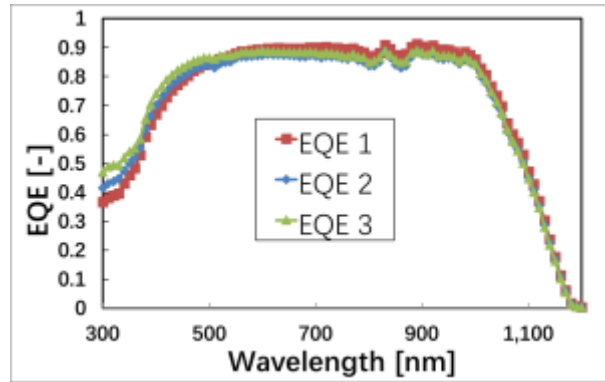


Figure 25 EQE curves of solar cells with different a-Si on FSF.

The difference in a-Si:H thickness on FSF does not cause much difference on J_{SC} if compare cell 1 and 3. However, EQE curves illustrate the effect caused by thinner a-Si:H at front side. The spectral response in short wavelength (<500 nm) become higher with the decrease of a-Si:H thickness which is shown in Figure 25. But the higher spectrum response in short wavelength does not promise a high J_{SC} , cell 1 has higher response in the wavelength between 600 nm and 1000 nm, as a consequence, cell 1 has higher J_{SC} than cell 2 and 3. The low V_{OC} value is mainly due to the partially textured c-Si surface. The rough surface induces a high surface recombination rate and hence a low V_{OC} .

The results of these three solar cells illustrate that thinner a-Si:H on FSF reduce the parasitic absorption in short wavelength range (<500 nm). However, the effect of thinner front a-Si:H on front surface passivation is not able to be drawn from this solar cell run. The reason is that the V_{OC} is affected by two variables: the thickness of a-Si:H and the rough emitter surface. As the rough emitter is detrimental to V_{OC} , the effect of different a-Si:H thickness is not obvious to be figured out. Thus, further experiments need to be done to eliminate the influence of process problem and control the variable for solar cells.

4.5 The influence of post annealing on cell performance

Different a-Si:H thickness at rear side of solar cells are tested in order to have better passivation on poly-Si. Since thicker PECVD a-Si:H means more hydrogen atoms are provided during the deposition and hence a better passivation, a-Si:H with different thickness which are 6.5 nm, 13 nm and 19.5 nm are deposited on the back side of the solar cell, while 6.5 nm is the thickness used in the previous solar cell. Solar cells in Table 8 are processed in the same run as solar cells in Table 7, so the undesired rough area on c-Si in emitter area also happened.

Table 8 Performance of solar cells with different a-Si:H at rear side with 22nm a-Si at front side.

Cell number	Area [cm ²]	Rear a-Si:H Thickness [nm]	V_{OC} [mV]	J_{SC} [mA/cm ²]	FF [%]	η [%]
1	9	6.5	665	38.2	73.5	18.7
2	9	13	674	39.8	75.7	20.3
3	9	19.5	671	39.3	74	19.6

The rough emitter is not only detrimental to V_{OC} , but also it reduces the FF. The values of V_{OC} and FF in Table 8 are not the data that measured right after the metallization and lift-off. The initial V_{OC} and FF is not as high as the values shown in the table. After annealing at 600 °C for several seconds, both V_{OC} and FF show a different degree of growth depending on the thickness of a-Si:H on the back side. Figure 26 reports the trends of V_{OC} and FF with annealing time.

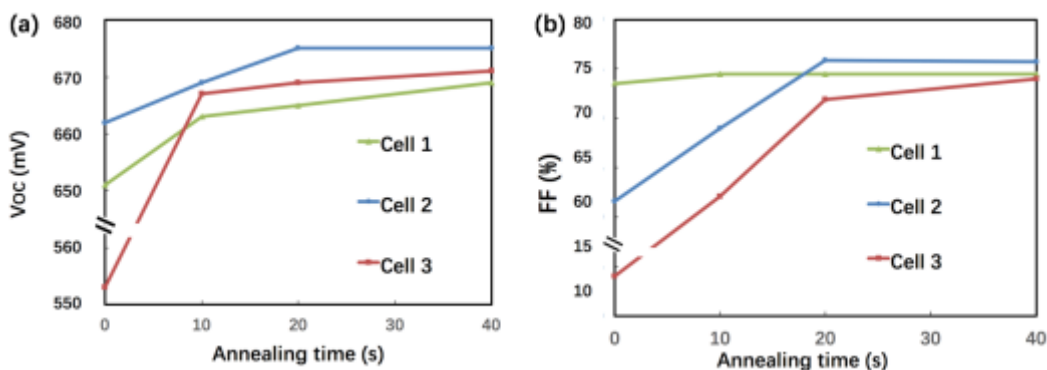


Figure 26 The effect of annealing time on (a) V_{OC} (b) FF at 600 °C in N_2 atmosphere.

The annealing takes place in N_2 atmosphere at 600 °C, all cells experienced step annealing, and cells are measured after 10s, 20s and 40s annealing. For cell 1, the change of V_{OC} and FF are not apparent after annealing. The difference after annealing becomes larger with the increase of a-Si:H thickness on the back side. To be specific, the initial V_{OC} and FF are only 554 mV and 14% for cell with 19.5 nm a-Si:H. The increase in V_{OC} after annealing may because hydrogen atoms are driven inside poly-Si and c-Si and provides passivation. The increase in FF is due to the formation of aluminum-silicon alloy at temperature higher than 577 °C [40], it decreases the FF contact resistance of Al/a-Si:H/poly-Si contacts. To verify the change of contact resistance, TLM measurements is carried out for both Al/a-Si:H/n-type poly-Si and Al/a-Si:H/p-type poly-Si with 19.5 nm a-Si:H in between. The contact resistance is measured before and after the annealing at 600 °C for 20s, the results after annealing are described in Figure 27. The measured resistances from dark J-V measurement are several thousand Ohm before annealing both for Al/a-Si:H/n-type poly-Si and Al/a-Si:H/p-type poly-Si samples, the results have poor linearity and it is impossible to obtain the contact resistance. Therefore, the contact resistance before annealing is not shown in Figure 27, it can be sure that resistance measured from dark J-V is several hundred times larger than that after annealing. Thus, the contact resistivity of Al/poly-Si contacts with 19.5 nm a-Si in between after annealing at 600 °C for 20s are about 1 $m\Omega/cm^2$ for n-type and 0.1 $m\Omega/cm^2$ for p-type. The values are much higher compared to the direct Al/poly-Si contacts, which are below 0.1 $m\Omega/cm^2$ for n^+ poly-Si and around $10^{-3} m\Omega/cm^2$ for p^+ poly-Si [33]. The high contact resistivity of Al/poly-Si contact after inserting a 19.5 nm a-Si:H induces a low FF compared to results in Table 6.

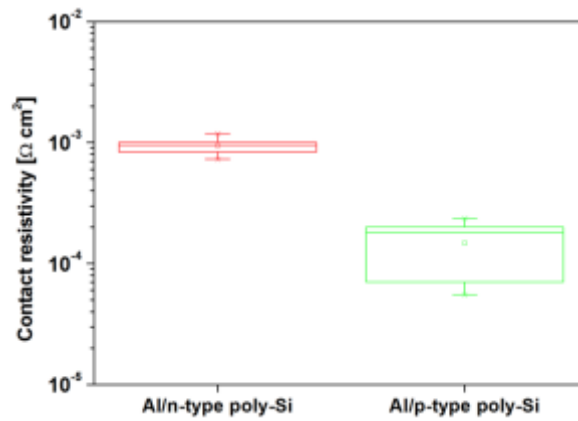


Figure 27 Contact resistivity of Al/a-Si:H/n-type poly-Si and Al/a-Si:H/p-type poly-Si contacts after annealing at 600 °C for 20s.

After annealing, the difference of V_{OC} and FF between cells becomes small. It means that thicker a-Si at back side does not provide better passivation since cell 3 does not have higher V_{OC} than cell 1 and 2, on the contrary, it will decrease the initial V_{OC} and FF. However, the back side a-Si:H in these three solar cells still only have contact with poly-Si in the metal contact area as shown in Figure 24 (b). The case of a-Si:H to poly-Si contact area on the cell performance still need to be investigated.

5

Conclusions and Recommendations

5.1 Conclusion

The focus of this thesis project is to optimize the IBC solar cells with poly-Si passivating contacts by means of improving the passivation properties of poly-Si and the front surface field, FSF.

Based on the previous study, it was found that the doping level and doping profile of the poly-Si layers are the most crucial parameters that affect their passivation properties [10]. Therefore, in this project, the ion-implantation dose for n-type and p-type doped poly-Si layers, which work as BSF and emitter in the n-type bulk IBC solar cells, are studied. Since the implanted dopants need to be driven in and activated by high-temperature annealing, the effect of two-step annealing, which is currently used for the process flow of poly-Si passivating contacts IBC solar cell, is investigated. Besides the optimization of poly-Si layers' doping and annealing steps, a tunnel oxide layer which gives more stable chemical passivation is developed in this work.

In order to quench the recombination loss in the front surface of the IBC solar cells, the passivation layers to the FSF, a-Si:H/SiN_x, are optimized, in terms of deposited temperature and thickness of the a-Si:H layer. For n-type bulk solar cell, phosphorous is the dopant for FSF. Then, the doping level for FSF, in terms of implantation dose, is also studied.

1. Passivating properties of poly-Si passivating contacts.

Field-effect passivation on BSF and emitter is optimized in two aspects: the doping level and doping profile, which are obtained by varying the implantation dose and annealing condition. The tunnel oxide is formed by standard cleaning process in Else Kooi laboratory in these two experiments, and it does not offer a stable chemical passivation. The standard cleaning is which is first a ten-minute immersion of wafers in 99%, room temperature HNO₃ and followed by five-minute rinsing in deionized (DI) water, then ten-minute immersion in 67.5%, 110 °C HNO₃ and followed by five-minute rinsing in DI water as well. When implantation dose for both BSF and emitter are at $4 \times 10^{15} / \text{cm}^2$, the best passivation is obtained, J_0 equals to 7.5 fA/cm² and 16 fA/cm² for n-type poly-Si and p-type poly-Si passivating contacts, separately. For the effect of annealing on the passivation, samples with no annealing after implantation show poor passivation. However, after annealing in O₂ atmosphere at 950 °C for 5 minutes, J_0 decreases to 5.7 fA/cm² for n-type poly-Si sample and 14.15 fA/cm² for p-type poly-Si sample. This is because of the fact that dopants are driven in and activated by energy provided in high-temperature annealing. Since the second annealing step is imperative for FSF in current IBC solar cell process, the influence of this second annealing on BSF and emitter is investigated. After O₂ atmosphere annealing, samples are annealed in N₂ atmosphere at 850 °C for 90 minutes. The results show a small effect on J_0 and V_{OC} but half the minority carrier lifetime.

2. A stable approach for tunnel oxide fabrication.

Tunnel oxide formation for poly-Si passivating contacts is optimized in this work. After the removal of native oxide on n-type float zone wafer, a one-hour 67.5% HNO₃ silicon oxidation is performed, which gives an excellent chemical passivation for c-Si. This process is done in a dedicated quartz container with fresh HNO₃ which is only prepared for tunnel oxide formation. For n-type poly-Si samples, the minority carrier lifetime is above 18 ms, J₀ equals to 4.5 fA/cm² and V_{OC} higher than 730 mV. For p-type poly-Si samples, the lowest J₀ is 12.9 fA/cm² and V_{OC} reaches 714 mV. The tunnel oxide formed in this way is supposed to have high thermal stability and provides good chemical passivation.

3. FSF doping and passivation.

Different phosphorous implantation dose with different a-Si:H deposition conditions are carried out on symmetrical test samples. The lowest J₀ for a textured n-FZ wafer is 6.5 fA/cm², with phosphorous implantation dose at $1 \times 10^{14}/\text{cm}^2$ and 22 nm thick a-Si:H deposited at 250 °C.

4. High efficiency IBC solar cells.

Solar cells with different structures are fabricated in this work. Solar cells with the same structure as Yang [10], achieve 83.2% FF on a 0.72 cm² which shows the solar cell has almost no shunt problem, the metal finger thickness was found to be the limiting factor of a low FF on 9 cm² scale cells. Al₂O₃ grown via ALD is deposited on poly-Si does not give a better passivation. Since the negative corona charge in Al₂O₃ is not a good option for n-type wafer. Solar cells with optimized NAOS and front passivation are fabricated. On the back side, a 6.5-nm thick layer a-Si:H deposited on poly-Si for chemical passivation enhancement. With optimized structure, the efficiency reaches 22.1% on a 0.72 cm² cell, with V_{OC}=709 mV, J_{SC}=40.7 mA/cm² and FF=76.4%. The low FF is due to the shunting induced by a-Si:H in the trench on the back side of the IBC solar cell. Therefore, with a thermal SiO₂ layer on rear side is formed for current isolation, the highest efficiency reaches 21.9% for 9 cm² cell, and 22.5% for 0.72 cm² cell. The thickness of a-Si:H on both front side and back side are also studied, for minimizing the front side parasitic absorption and obtaining high passivation. It is proved experimentally that a thinner a-Si:H on front side can reduce parasitic absorption and enhance the short wavelength light response. The thicker a-Si:H on rear side induces high series resistance in solar cell which limits the cell FF. The high series resistance is caused by high contact resistance in Al/a-Si:H/poly-Si contacts and it will lower the initial V_{OC} and FF. This problem can be reduced by 20-second annealing at 600 °C due to the formation of aluminum-silicon alloy at the temperature higher than 577 °C [40].

5.2 Recommendations

To further enhance the efficiency of IBC solar cells poly-Si passivating contacts, several optimizations can be performed.

1. Reducing parasitic absorption on both short and long wavelength, and double anti-reflection coating for J_{SC} enhancement.

The difference in EQE and 1-R-T curves in Figure 23 (a) shows that solar cells still suffer high parasitic absorption in both short wavelength (<500 nm) and long wavelength (>1000 nm). Therefore, the deposition condition of a-Si:H can be further improved by using a thinner layer on front side while dose not destroy the passivation performance. Meanwhile, materials with lower absorption coefficient at long wavelength, such as in-situ doped PECVD poly-SiO_x [8], can be the alternatives for LPCVD a-Si for lowering parasitic absorption at long wavelength. The slope at the wavelength between 600 nm and 1000 nm in Figure 23 (a) indicates that double anti-reflection coating can be implemented on solar cells

for further enhance the J_{SC} . For example, a thin layer of MgF_2 or SiO_2 can be deposited on SiN_x at the front side for optical performance enhancement.

2. Thermal SiO_2 formation and patterning on back side of the solar cell.

Thermal SiO_2 on BSF and emitter can be etched like it is shown in Figure 24 (a), this structure can promise a good passivation on the rear side and prevent current shunt problem. The passivation on the trench between BSF and emitter is important as the high carrier flow density near the gap surface. Therefore, the way of thermal oxide formation at the trench can be studied, such as wet thermal oxide or dry thermal oxide.

3. Improvement of the solar cell process flow.

In the process flow developed in PVMD groups, there are two LPCVD a-Si etching steps. The a-Si of emitter is deposited on the etched c-Si, this affects the passivation of p-type poly-Si passivating contacts. The process flow can be improved with only one LPCVD a-Si etching step, where only a-Si between BSF and emitter is removed. The cell structure with improved process flow is shown in Figure 28 where there is no height difference between BSF and emitter. No c-Si etching under emitter promises the best chemical passivation for p-type poly-Si passivating contacts and gives rise to solar cell efficiency.

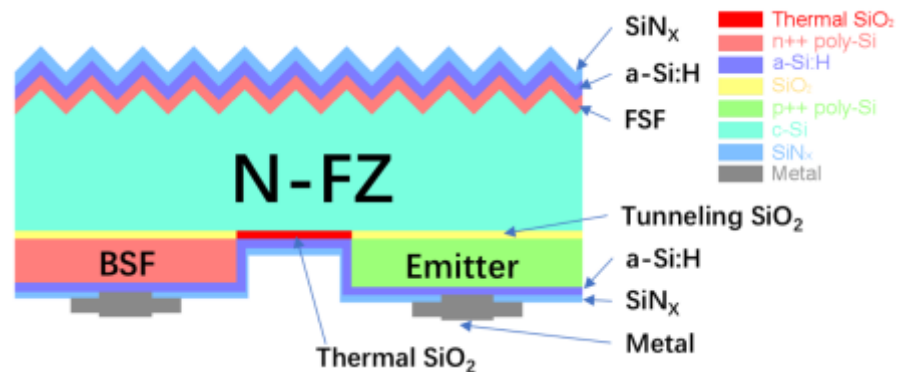


Figure 28 Schematic of the structure of the IBC solar cell with poly-Si passivating contacts with the improved process flow.

4. SiO_2/SiN_x passivation layers at rear side of the solar cell for internal reflection, and the different SiN_x at front and back side for high passivation and low front reflection.

The PECVD SiO_2 layer can be deposited between a-Si:H and SiN_x for the high internal reflection in solar cell as SiO_2 has refractive index around 1.4. The enhancement in internal reflection can minimize the difference between 1-R and 1-R-T curves in Figure 23 (a) in long wavelength. The implement of this PECVD SiO_2 layer requires further experiments done regards its physical properties, such as thickness and deposition temperature, and the influence on passivation. Meanwhile, SiN_x layer can also be optimized in terms of the stoichiometry. Since N rich SiN_x layer has refractive index around 2 and with high charge density. The high interface charge density always corresponds to the high interface state. The Si rich SiN_x has high refractive index but it has high hydrogen contents (see Figure 29), therefore, the passivation of Si rich SiN_x is dominated by chemical passivation [49]. In our IBC solar cell, N rich SiN_x can be used as anti-reflection coating on the front side for better spectral response, while Si rich SiN_x can replace the back side SiN_x in our solar cell for high passivation.

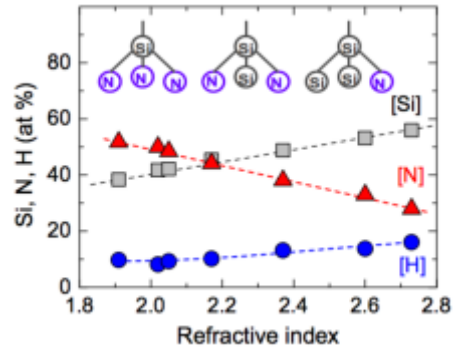


Figure 29 The relation of H, Si, and N density and refractive index in a-SiN_x:H [40].

5. Black silicon and passivation layer at front side.

Black silicon can also be implemented on the front surface for enhance the J_{sc} . However, the fabrication of black silicon is the result of multi-texturing which requires high quality passivation on front side. Then, the black silicon in combination with the passivation layer on it can be further investigated.

6. Screen printing for thicker metal fingers and high FF.

In both section 4.2 and 4.3, 0.72 cm² solar cells have higher FF than that of 9 cm² cells indicates that the resistance of the metal fingers at the rear side limits the solar cell efficiency. In current process of our IBC solar cells, the patterning of metal fingers is done by photolithography and then lift-off. A thick metal finger requires at least twice thick photoresist for the convenience of lift-off. The lift-off is also relevant to the aspect ratio of the metal finger. Consequently, a thick metal finger is not easy to achieve by means of photolithography and lift-off process. Therefore, screen printing can be the alternative for the metal deposition which allows growing thick metal fingers.

7. Optimization of annealing condition for high passivation and low thermal budget.

In section 3.2, the results of the experiment show that the second annealing, which is a 90-minute annealing in N₂ atmosphere at 850 °C, half the lifetime of both n-type poly-Si and p-type poly-Si samples, while the J_0 shows slightly increase and $i-V_{oc}$ decrease. Therefore, the second annealing condition can be optimized with its effect on FSF passivation. As the dopants in FSF should be kept in the shallowest region to obtain the best passivation [40]. The annealing with shorter time and lower temperature can be tested which has three advantages: 1. reducing the impact on emitter and BSF passivation; 2. shallow dopants profile in FSF may lead to high FSF passivation; 3. lower temperature and shorter annealing time decrease the thermal budget.

8. Further research on the formation of tunnel oxide and its impact on passivation for poly-Si passivating contacts.

As the physic properties, which are the thickness, density, and stoichiometry, of tunnel silicon oxide are affected by the condition of nitric acid solution, such as temperature and concentration, and the immersion. The way of the formation for tunnel oxide may also influence its thermal stability, and hence impacts the chemical passivation. Thus, further experiments regarding the tunnel oxide physical properties and passivation performance deserves to be done for higher solar cell efficiency.

With optimizations mentioned above, we believe the solar cell efficiency will boost to at least 23% in short term.

Bibliography

- [1] BP Statistical Review of World Energy June 2016. Available:
<http://www.bp.com/content/dam/bp/pdf/energy-economics/statistical-review-2016/bp-statistical-review-of-world-energy-2016-full-report.pdf>.
- [2] Perez, R. and M. Perez, A fundamental look at energy reserves for the planet. *The International Energy Agency SHC Programme Solar Update*, Vol. 50, 2-3, 2009.
- [3] Arnulf Jäger-Waldau, PV Status Report 2016, Available on line on:
<http://publications.jrc.ec.europa.eu/repository/bitstream/JRC103426/Idna28159enn.pdf>.
- [4] A. Smets et al., *Solar Energy: The Physics and Engineering of Photovoltaic Conversion, Technologies and Systems*, UIT Cambridge Ltd., 2016.
- [5] M. Aleman, L. Tous, E. Cornagliotti, F. Duerinckx, J. John, N.E. Posthuma, R. Russell, S. Singh, E. Sneeckx, A. Uruena, J. Szlufcik, Large-Area High-Efficiency n-type Rear Junction Cells Featuring Laser Ablation and Cu-plated front contacts, *EUPVSEC*, 2013.
- [6] M. Green, *Solar cells: Operating principles, technology and system applications*, Univ. New South Wales, 1998.
- [7] A. Richter, M. Hermle, S. W. Glunz, Improved quantitative description of Auger recombination in crystalline silicon, *IEEE J. Photovoltaics*, Vol. 3, 1184, 2013.
- [8] Guangtao Yang, Yue Zhang, Paul Procel, Arthur Weeber, Olindo Isabella, Miro Zeman, Poly-Si(O)_x passivating contacts for high-efficiency c-Si IBC Solar cell, *Energy Procedia*, accepted for publication.
- [9] Dauwe S, Schmidt J, Hezel R, Very low surface recombination velocities on p- and n-type silicon wafers passivated with hydrogenated amorphous silicon films, *Proceedings of the 29th IEEE Photovoltaic Specialists Conference*, New Orleans, USA, 2002; 1246-1249.
- [10] Guangtao Yang, Andrea Ingenito, Olindo Isabella, Miro Zeman, IBC c-Si solar cells based on ion-implanted poly-silicon passivating contacts, *Solar Energy Materials and Solar Cells*, Vol. 15, 884-90, 2016.
- [11] Guangtao Yang, Andrea Ingenito, Nienke van Hameren, Olindo Isabella, Miro Zeman, Design and application of ion-implanted polySi passivating contacts for interdigitated back contact c-Si solar cells, *Applied Physics Letter*, Vol. 108, 033903, 2016.
- [12] Dauwe S, Mittelstädt L, Metz A, Hezel R, Experimental evidence of parasitic shunting in silicon nitride rear surface passivated solar cells, *Progress in Photovoltaics*, Vol. 10, 271-278, 2012.
- [13] J. Schmidt, J. D. Moschner, J. Henze, S. Dauwe and R. Hezel, Recent progress in the surface passivation of silicon solar cells using silicon nitride, *European Photovoltaic Solar Energy Conference*,

2004, Paris, France.

- [14] Agostinelli G, Delabie A, Vitanov P, Alexieva Z, Dekkers HFW, De Wolf S, Beaucarne G, Very low surface recombination velocities on p-type silicon wafers passivated with a dielectric with fixed negative charge, *Energy Materials and Solar Cells*, Vol. 90, 3438– 3443, 2006.
- [15] J. Schmidt, A. Merkle, R. Brendel, B. Hoex, M. C. M. van de Sanden, W. M. M. Kessels, Surface passivation of high-efficiency silicon solar cells by atomic-layer-deposited Al₂O₃, *Prog. Photovolt: Res. Appl.*, Vol. 16:461–466, 2008.
- [16] W.M.M. Kessels, J.A. van Delft, G. Dingemans, and M.M. Mandoc, Review on the prospects for the use of Al₂O₃ for high-efficiency solar cells, Workshop (Dept. of Applied Physics, Eindhoven University of Technology (TU/e), The Netherlands).
- [17] B. Hoex, J. Schmidt, P. Pohl, M. C. M. van de Sanden, and W. M. M. Kessels, Silicon surface passivation by atomic layer deposited Al₂O₃, *Journal of Applied Physics*, Vol. 104, 044903, 2008.
- [18] S. A. McHugo, H. Hiesimair, and E. R. Weber, Gettering of metallic impurities in photovoltaic silicon, *Applied Physics A: Materials Science and Processing*, Vol. 64, 127, 1997.
- [19] S. W. Glunz, S. Rein, J. Y. Lee, and W. Warta, Minority carrier lifetime degradation in boron-doped Czochralski silicon, *Journal of Applied Physics*, Vol. 90, 2397, 2001.
- [20] Andrew W, Blakers, Aihua Wang, Adele M, Milne, Jianhua Zhao, Martin A Green, 22.8 % efficient silicon solar cell, *Appl. Phys. Lett.* Vol. 55, 1363, 1989.
- [21] J. Zhao, A. Wang and M.A. Green, 24.5% efficiency silicon PERT Cells on MCZ substrates and 24.7% efficiency PERL cells on FZ substrates, *Prog. Photovolt: Res. Appl.* Vol. 7, 471-474, 1999.
- [22] Jimmy Melskens, Bas W. H. van de Loo, Bart Macco, Martijn F. J. Vos, Jurgen Palmans, Sjoerd Smit, W. M. M. (Erwin) Kessels, Concepts and Prospects of Passivating Contacts for Crystalline Silicon Solar Cells, *IEEE PVSC*, New Orleans, LA, 2015.
- [23] Mikio Taguchi, Ayumu Yano, Satoshi Tohoda, Kenta Matsuyama, Yuya Nakamura, Takeshi Nishiwaki, Kazunori Fujita, and Eiji Maruyama, 24.7% Record Efficiency HIT Solar Cell on Thin Silicon Wafer, *IEEE Journal of Photovoltaic*, Vol. 4, No. 1, January 2014.
- [24] Frank Feldmann, Maik Simon, Martin Bivour, Christian Reichel, Martin Hermle, Stefan W. Glunz, Efficient carrier-selective p- and n-contacts for Si solar cells, *Solar Energy Materials & Solar Cells*, Vol. 131, 100–104, 2014.
- [25] T. Matsushita, T. Aoki, T. Otsu, H. Yamoto, H. Hayashi, M. Okayama, and Y. Kawana, “Semi-insulating polycrystalline- silicon (SIPOS) passivation technology,” *Proceedings of the 7th Conference on Solid State Devices*, Tokyo, Japan, 1975.
- [26] E. Yablonovitch, T. Gmitter, R.M. Swanson, Y.H. Kwark, A 720 mV open circuit voltage SiO_x:c-Si:SiO_x double heterostructure solar cell, *Appl. Phys. Lett.* Vol. 47, 1211, 1985.
- [27] Tao Y, Upadhyaya V, Huang Y, Chen C, Jones K, Rohatgi A, Carrier selective tunnel oxide passivated contact enabling 21.4% efficient large-area n-type silicon solar cells. In: *43rd IEEE Photovoltaic Specialists Conference*; June 5; Portland, Oregon; 2016.

- [28] P. Koswatta, M. Boccard, and Z. Holman, "Carrier-Selective Contacts in Silicon Solar Cells," no. 2, 1–4, 2015.
- [29] R. Peibst, U. Römer, Y. Larionova, M. Rienacker, A. Merkle, N. Folchert, S. Reiter, M. Turcu, B. Min, J. Krugener, D. Tetzlaff, E. Bugiel, T. Wietler, R. Brendel, Working principle of carrier selective poly-Si/c-Si junctions: Is tunnelling the whole story?, *Sol. Energy Mater. Sol. Cells*, Vol. 158, 60–67, 2016.
- [30] S. W. Glunz, F. Feldmann, A. Richter, M. Bivour, C. Reichel, H. Steinkemper, J. Benick, M. Hermle, The Irresistible Charm of a Simple Current Flow Pattern – 25% with a Solar Cell Featuring a Full-area Back Contact. *In Proc, 32nd EU PVSEC*, Hamburg, Germany, 2015.
- [31] Keiichiro Masuko, Masato Shigematsu, Taiki Hashiguchi, Daisuke Fujishima, Motohide Kai, Naoki Yoshimura, Tsutomu Yamaguchi, Yoshinari Ichihashi, Takahiro Mishima, Naoteru Matsubara, Tsutomu Yamanishi, Tsuyoshi Takahama, Mikio Taguchi, Eiji Maruyama, and Shingo Okamoto, Achievement of more than 25% conversion efficiency with crystalline silicon heterojunction solar cell. *IEEE Journal of Photovoltaics*, Vol. 4, No. 6, 2014.
- [32] Kaneka, Press release (14th Sept. 2016), http://www.kaneka.co.jp/kaneka-e/images/topics/1473811995/1473811995_101.pdf.
- [33] Michael Rienacker, Marcel Bossmeyer, Agnes Merkle, Udo Römer, Felix Haase, Jan Krügener, Rolf Brendel, and Robby Peibst, Junction Resistivity of Carrier-Selective Polysilicon on Oxide Junctions and Its Impact on Solar Cell Performance, *IEEE Journal of Photovoltaic*, Vol. 7, NO. 1, 2017.
- [34] A. Ingenito, O. Isabella, M. Zeman, Simplified process for high efficiency, self-aligned IBC c-Si solar cells combining ion implantation and epitaxial growth: design and fabrication, *Solar Energy Materials & Solar Cells*, Vol. 157, 354–365, 2016.
- [35] Fridman. Contact resistance and TLM measurements, 1–11, 2014. Available: http://tuttle.merc.iastate.edu/ee432/topics/metals/tlm_measurements.pdf.
- [36] Ronald A. Sinton, Andres Cuevas, Contactless determination of current–voltage characteristics and minority-carrier lifetimes in semiconductors from quasi-steady-state photoconductance data, *Appl. Phys. Lett.* Vol. 69, 2510, 1996.
- [37] R.A. Sinton, A. Cuevas, M. Stuckings, Quasi-steady-state photoconductance, a new method for solar cell material and device characterization, in: *Proceedings of the 25th IEEE Photovoltaic Specialists Conference, IEEE*, New York, NY, USA, Washington DC, USA, 1996, 457–460.
- [38] Frank Feldmann, Christian Reichel, Ralph Müller, Martin Hermle, The application of poly-Si/SiO_x contacts as passivated top/rear contacts in Si solar cells, *Solar Energy Materials & Solar Cells*, Vol. 159, 265–271, 2017.
- [39] Christian Reichel, Frank Feldmann, Ralph Müller, Robert C. Reedy, Benjamin G. Lee, David L. Young, Paul Stradins, Martin Hermle, Stefan W. Glunz, Tunnel oxide passivated contacts formed by ion implantation for applications in silicon solar cells, *Journal of Applied physics*, Vol. 118, 205701, 2015.
- [40] Shaoqing Xiao, Shuyan Xu, High-Efficiency Silicon Solar Cells—Materials and Devices Physics,

Critical Reviews in Solid State and Materials Sciences, Vol. 39, 277–317, 2014.

[41] Jan Krügener, Robby Peibst, Eberhard Bugiel, Dominic Tetzlaff, Fabian Kiefer, Marcel Jestremski, Rolf Brendel, Jörg Osten, Ion implantation of boric molecules for silicon solar cells, *Solar Energy Materials & Solar Cells*, Vol. 142, 12–17, 2015.

[42] Frank Feldmann, Ralph Müller, Christian Reichel, and Martin Hermle, Ion implantation into amorphous Si layers to form carrier-selective contacts for Si solar cells, *Phys. Status Solidi RRL*, Vol. 8, No. 9, 767–770, 2014.

[43] M.M. Mandurah, K.C. Saraswat, C.R. Helms, T.I. Kamins, Dopant segregation in polycrystalline silicon, *J. Appl. Phys.* Vol. 51, 5755, 1980.

[44] T. Yamamoto, K. Uwasawa, T. Mogami, Bias temperature instability in scaled p/sup +/- polysilicon gate p-MOSFET's, *IEEE Trans. Electron Devices*, Vol. 46, 921, 1999.

[45] Corsin Battaglia, Andres Cuevas, Stefaan De Wolf, High-efficiency crystalline silicon solar cells: status and perspectives, *Energy Environ. Sci.*, Vol. 9, 1552, 2016.

[46] Anamaria Moldovan, Frank Feldmann, Martin Zimmer, Jochen Rentsch, Jan Benick, Martin Hermle, Tunnel oxide passivated carrier-selective contacts based on ultra-thin SiO₂ layers, *Solar Energy Materials & Solar Cells*, Vol. 142, 123–127, 2015.

[47] Hikaru Kobayashi, Asuha, Osamu Maida, Masao Takahashi, Hitoo Iwasa, Nitric acid oxidation of Si to form ultrathin silicon dioxide layers with a low leakage current density, *Journal of Applied Physics*, Vol. 94, 7328, 2003.

[48] U. Römer, R. Peibst, T. Ohrdes, B. Lim, J. Krügener, E. Bugiel, T. Wietler, R. Brendel, Recombination behavior and contact resistance of n⁺ and p⁺ poly-crystalline Si/mono-crystalline Si junctions, *Sol. Energy Mater. Sol. Cells*, 131, 85–91, 2014.

[49] G. Dingemans, W. M. M. Kessels, Status and prospects of Al₂O₃-based surface passivation schemes for silicon solar cells, *J. Vac. Sci. Techno. A.*, Vol. 30, 040802, 2012.